Magnetic field and ion-optical simulations for the optimization of the Super-FRS

Magnetfeld- und ionenoptische Simulationen für die Optimierung des Super-FRS
Zur Erlangung des Grades eines Doktors der Naturwissenschaften (Dr. rer. nat.)
genehmigte Dissertation von Erika Kazantseva aus Chirchik/UdSSR
Tag der Einreichung: 21.01.2019, Tag der Prüfung: 29.04.2019
Darmstadt — D 17

1. Gutachten: Prof. Dr. Oliver Boine-Frankenheim
2. Gutachten: Prof. Dr. Christoph Scheidenberger

TECHNISCHE UNIVERSITÄT DARMSTADT

Fachbereich Elektrotechnik und Informationstechnik
Institut für Teilchenbeschleunigung und Elektromagnetische Felder

Magnetic field and ion-optical simulations for the optimization of the Super-FRS
Magnetfeld- und ionenoptische Simulationen für die Optimierung des Super-FRS

Genehmigte Dissertation von Erika Kazantseva aus Chirchik/UdSSR

1. Gutachten: Prof. Dr. Oliver Boine-Frankenheim
2. Gutachten: Prof. Dr. Christoph Scheidenberger

Tag der Einreichung: 21.01.2019
Tag der Prüfung: 29.04.2019

Darmstadt — D 17

Erklärung zur Dissertation

Hiermit versichere ich, die vorliegende Dissertation ohne Hilfe Dritter und nur mit den angegebenen Quellen und Hilfsmitteln angefertigt zu haben. Alle Stellen, die aus Quellen entnommen wurden, sind als solche kenntlich gemacht. Diese Arbeit hat in gleicher oder ähnlicher Form noch keiner Prüfungsbehörde vorgelegen.

Darmstadt, den 21. Januar 2019

(Erika Kazantseva)

Contents

1 Introduction

The Nuclear Structure Astrophysics and Reactions (NUSTAR) collaboration program [1, 2] is one of the four research pillars of the FAIR project [3, 4]. The main focus of the NUSTAR experiments is the investigation of exotic nuclei, which will be produced and separated in-flight [5] by means of the Superconducting Fragment Separator (Super-FRS) [6, 7]. The quality of the separation and transmission rates of the Super-FRS have a direct impact on the success of NUSTAR and FAIR. To operate the Super-FRS effectively, it is required to have a realistic model for simulating and optimizing of parameters for various beam rigidities.

There are many different possibilities to simulate the motion of a charged particle in electromagnetic fields. They are all based on the solution of the equations of motion. Since in general the analytical solution cannot be derived for the real fields, numerical integration of the equations of motion is required. The secondary ion beams in separators are not intense[1], and space charge effects [8] can be neglected [6]. Thus, the description of single-particle motion suffices for the modelling of a separator. Unlike for synchrotrons, where a beam passes through the same field millions of times and where it is crucial to preserve the symplecticity [9, 10], separators are single-pass systems and it is important to consider the full equations of motion, derived from the full (i.e. not linearized) Hamiltonian. The numerical solution of such equations of motion for each particle in a 3D realistic field distribution (*tracking*) is the most accurate way to describe the particle dynamics in separators. Nevertheless, tracking individual particles is a computationally expensive procedure, which is still too slow to be used for operational control and settings optimization. A well established approach for the fast simulation of an accelerator system is the ion-optical approach [11], where the motion of the beams through the electromagnetic fields is described by Taylor transfer maps and by the reference trajectory. The transfer maps are polynomial operators, which relate the initial and final positions of the particles in the phase volumes between two points along the reference path [10, 11]. The larger is the fraction of the aperture of

[1] In the Super-FRS case, which is on the frontier of the secondary beam intensity, the maximal beam intensity of $3 \cdot 10^{11}$ ions in a pulse of 50 ns is expected in the first preseparator stage [7].

the ion-optical elements which is illuminated by the beam, the higher should be the order of the transfer map to provide an accurate prediction of the particle dynamics. For iron-dominated separators with a wide rigidity range, the saturation of the iron yokes leads to changes in the magnetic field and the particle dynamics. To maintain the predictability of the ion-optical model, these effects have to be considered as well.

The main focus of this work was to develop a general and robust approach to generate realistic Taylor transfer maps for large aperture accelerator magnets starting from magnetic field simulations or measurements. Nowadays, besides the integration of equations of motion in the differential algebraic (DA) framework [12, 10], there are several different state of the art methods to generate transfer maps of arbitrary field distributions. The most relevant among them are the method of Tracking particles and Fitting Coefficients (TRAFIC) [13, 14] as well as analytical [15] and numerical [14] integration of the expressions for individual transfer map elements, derived from the Taylor-expanded equations of motion. While the straight-forward TRAFIC method is principally capable to find accurate transfer maps, it is not very convenient for high orders due to large computational effort. Fitting of small groups of the transfer map elements separately might not work for systems with complex field distributions. Elementwise approximations of transfer maps via analytical/numerical integration is suitable for low orders, but the increasing number of elements with the growth of the order makes it hardly possible to derive all extremely long corresponding expressions. Both methods with integration of elements require the knowledge of the magnetic field derivatives up to the considered order. Utilizing the least squares methods for the computation of the magnetic field derivatives in [14] is a useful concept, which finds an application in this work.

Within this work the Surface Integration Helmholtz Method (SIHM), developed in [16, 17], was exploited and extended for considering flat volumes of interest and the rigidity dependency of the transfer maps. Different surface approximation methods were tested using a simple analytical model as a benchmark. As an example the methods were applied to the normal conducting radiation-resistant dipole magnet of the Super-FRS preseparator with design deflection angle $\theta_0 = 11^\circ$ and design radius $R_0 = 12.5\,\mathrm{m}$ [18]. Therefore, a 3D magnetostatic simulation using the measured magnetization curve of a material sample of the dipole yoke was performed. Finally, an ion-optical study of the Super-FRS preseparator with the derived rigidity dependent transfer maps was conducted.

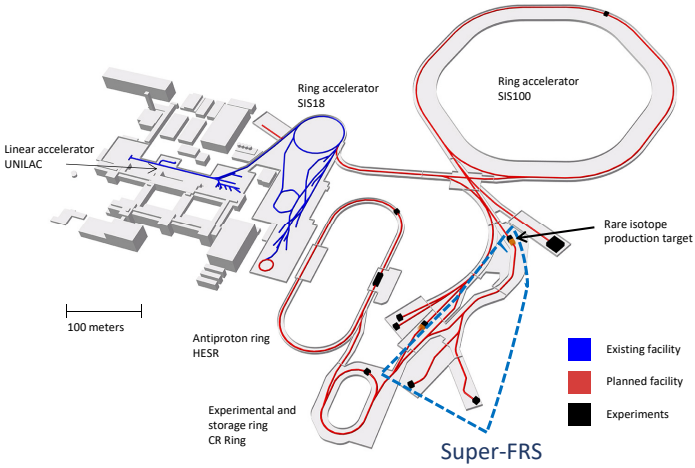

Figure 1.1: Schematic layout of the existing GSI and planned FAIR facility. The Super-FRS is marked with a dashed frame. (The picture is adapted from [4].)

The computations in this work were carried out using CST EMS [19], COSY INFINITY [20] and the Python programming language. The computations in this thesis are performed using double precision floating point arithmetics and the quantities in this work are presented in SI units. All polynomial evaluations were performed using the Horner scheme [21].

The Super-FRS project

The Super-FRS will be the most powerful in-flight projectile fragment separator and is currently being built at GSI [3, 22] for the FAIR project. In Fig. 1.1 the present GSI facility together with the planned FAIR facilities are shown. The location of the Super-FRS is marked with a dashed line frame. The Super-FRS has the same separation principle ($B\rho - \Delta E - B\rho$ principle) and goal momentum resolution as the existing FRS [23] facility at GSI, but a larger rigidity range, momentum and angular acceptance and a better transmission for the products of uranium fission. The ion-optical layout of the Super-FRS consists of two $B\rho - \Delta E - B\rho$ separators: the preseparator and the main separator. The secondary ions, produced via fragmentation or fission of the relativistic projectile beam on a production target are separated in the dipoles by their momentum-

to-charge ratio and in precisely shaped wedge energy degraders [24] by their atomic charge Z. Thus, the Super-FRS allows a full spatial separation of the nuclides up to ^{238}U. The main separator contains three different experimental branches: the low-energy branch which can be used as both high resolution magnetic spectrometer [25] and energy-buncher [26], the high-energy branch, and the ring branch.

Overview

The core of this thesis is composed of five chapters. In Chapter 2 the most important theoretical principles as well as numerical methods are summarized. In Chapter 3 the aspects of magnetic field simulation and measurement are illuminated using the example of a normal conducting 11° dipole magnet for the Super-FRS preseparator. The simulated magnetic field is compared with the measurements. The saturation effects are demonstrated using the simulations. Chapter 4 contains the description of the developed method to obtain the functional dependence of the magnetic field on coordinates and excitation currents, accurately representing the B-field and satisfying the Laplace equation. A benchmarking and robustness testing using the analytical magnetic model as well as an application to the preseparator dipole magnet can be also found in this chapter. The subject of Chapter 5 is the generation of Taylor transfer maps starting from measured or simulated magnetic field data. Two different ways to obtain transfer maps utilizing magnetic field information are discussed together with aspects of the choice of the reference trajectory in a symmetric dipole. A method to obtain rigidity-dependent transfer maps of iron-dominated magnets is presented. Finally, the general approach for the transfer maps computation is verified using the analytical model introduced in Sec. 4.1. In Chapter 6 generated realistic transfer maps are applied to the ion-optical model of the Super-FRS preseparator. A study and optimization of the multipole strengths was conducted for both, the separator mode and the spectrometer mode. The effect of errors in the coil currents was discussed. The transfer maps, obtained using the different methods are compared in the context of the Super-FRS preseparator optics. The last chapter summarizes the results, obtained in the previous chapters.

2 Fundamentals

This chapter summarizes the theoretical background, methods and tools used in this work. The vector quantities are marked with arrows. For a better readability of the text, for defined vectors, the absolute value of a vector will be often defined by the corresponding symbol without an arrow, e.g., for $\vec{a}$, $a := |\vec{a}|$.

2.1 Motion of charged particles in electromagnetic fields

The motion of a charged particle with momentum $\vec{p}$, charge q, mass m and velocity $\vec{v}$ in an electromagnetic field is driven by the Lorentz force

$$\vec{F} = \frac{d\vec{p}}{dt} = q\left(\vec{E} + \vec{v} \times \vec{B}\right), \tag{2.1}$$

where $\vec{E}$ and $\vec{B}$ denote the electric field strength and the magnetic flux density, respectively. A relativistic particle has the momentum

$$\vec{p} = \gamma m \vec{v},$$

where

$$\gamma = 1/\sqrt{1 - v^2/c^2}$$

is the relativistic factor and c is the speed of light in vacuum. Often the ratio of the velocity to the speed of light

$$\beta = v/c$$

is used. In a constant magnetic field, perpendicular to the particle motion, the trajectories of charged particles form circles. Combining the centripetal acceleration and the magnetic term of Eq. (2.1), leads to

$$\gamma m v^2/R = q v B,$$

from which the radius of the circle is

$$R = \gamma m v/(qB) = p/(qB).$$

An important property of an accelerated charged particle is the magnetic rigidity, which will be denoted as $B\rho$ throughout this writing,

$$B\rho = B \cdot R = \frac{p}{q} \ [\mathrm{Tm}]. \tag{2.2}$$

It should be noted here, that $B\rho$ is a single variable (sometimes also denoted as χ_m) which corresponds to a commonly used notation in accelerator physics community [27]. For planar motion, which is usually the case in accelerator physics, the magnetic rigidity of a particle gives the information about the deflection radius in a given vertical magnetic field.

2.2 Accelerator magnets

The motion of charged particles in accelerators is determined by the Lorentz force Eq. (2.1). Whereas electric fields must be used for the acceleration of charged particles, they are not suitable for the steering of particles with relativistic momenta [28] due to the occurrence of discharges at the required field strengths. Therefore, the steering and focusing of relativistic particle beams is mostly done by magnetic fields. In accelerators three principally different types of the magnets are used: permanent magnets, iron-dominated, and coil-dominated magnets. Here only iron-dominated magnets will be discussed.

2.2.1 Iron-dominated dipole magnets

Iron-dominated magnets are electromagnets with soft-magnetic steel yokes used to produce the magnetic field with the desired properties. The surface of the steel with a high relative magnetic permeability μ_r is acting as an equipotential surface due to the continuity of the magnetic flux density and the magnetic Gauss's law

$$B_{n2} = B_{n1}, \tag{2.3}$$

$$\nabla \cdot \vec{B} = 0. \tag{2.4}$$

Here B is the magnetic flux density while the indices $n1$, $n2$ mean normal components in iron and air/vacuum, respectively. Further on B will be often named magnetic field or B-field for simplicity. The yoke surfaces, used to build up the field, are named pole shoes.

The main properties of the dipole magnet are the design deflection angle θ_0 and radius R_0, effective length $L_{\text{eff}} \approx \theta_0 \cdot R_0$ and the range of the main field B_0. In a dipole magnet the reference particle with a magnetic rigidity $B\rho = B_0 \cdot R_0$ is deflected by an angle $\theta_0 = L_{\text{eff}}/R_0$.

To find the coil current I required for the magnetic field B_0 in the pole gap, a rough estimate can be derived from Ampere's law

$$\oint_C \vec{H} \cdot d\vec{l} = nI, \tag{2.5}$$

where C is an arbitrary path enclosing both current coils as well as the pole gap, and n is the number of coil turns as shown in Fig. 2.1. The left part of Eq. (2.5) can be split into two integrals: one along the path in the yoke and one in the pole gap. Splitting the integrals and substituting

$$\vec{B} = \mu\vec{H} = \mu_0\mu_r\vec{H}$$

with the vacuum permeability $\mu_0 = 4\pi \cdot 10^{-7}$ Tm/A and a relative permeability $\mu_r = \mu/\mu_0$ leads to

$$\oint_C \vec{H} \cdot d\vec{l} = \int_{\text{yoke}} \frac{\vec{B}(l)}{\mu_0\mu_r^{\text{yoke}}(l)} \cdot d\vec{l} + \int_{\text{gap}} \frac{\vec{B}(l)}{\mu_0\mu_r^{\text{gap}}(l)} \cdot d\vec{l}. \tag{2.6}$$

In a vacuum gap with size h the relative permeability $\mu_r^{\text{gap}} = 1$, whereas $\mu_r^{\text{yoke}} \gg 1$ for iron yokes. Assuming that B does not change along the pole gap results in a final rule used as a rough estimate

$$B_{\text{gap}}h \approx \mu_0 nI. \tag{2.7}$$

Thus the distance between the opposite pole shoes together with the coil current and total number of conductor turns around both pole shoes are the main parameters defining the B-field magnitude in the magnet aperture.

Of course in reality the integral of $\vec{H}$ through the yoke does not vanish and for a detailed field solution Maxwell's equations have to be solved more precisely.

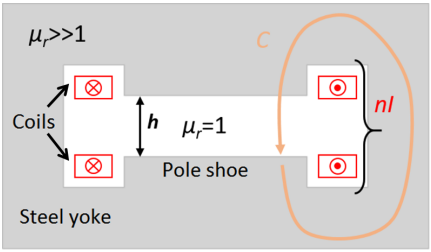

Figure 2.1: An illustration to Ampere's law in a dipole magnet.

Moreover, the magnetic saturation of the yoke leads to a decrease of the relative permeability with increasing H, making the term $\int_{\text{yoke}} \vec{H} \cdot d\vec{l}$ in Eq. (2.6) even more important.

2.2.2 Measurements and simulations of accelerator magnets

Since the motion of the particles is directly affected by the magnetic field distribution, the knowledge of the magnetic field is very important for accelerator design and operation. Whereas for the first accelerators it was sufficient to perform the design based on simplified analytical models (implying an infinite relative magnetic permeability μ for the yoke), with increasing energy of the accelerated particles and universality of the machines, the necessity of numerical simulation models increased rapidly. For the operation of the accelerators, magnetic measurements are still nearly irreplaceable, but precise 3D simulation models are becoming an alternative, since compared to measurements simulation takes much less effort and can be repeated and improved at any time.

A good simulation model should rely on realistic material properties of the yoke material and a careful implementation of the involved physical laws. However, the magnetization of ferromagnetics used for most accelerator magnets is a complicated hysteretic process with a nonlinear dependency on a variety of parameters like the magnetic field strength, ramping rate, mechanical stress and temperature [29]. This causes problems for both simulations and measurements.

To partially resolve the hysteresis issue, the following rules for measurements and operation are commonly used in the accelerator community:

1. Only one hysteresis branch is used.
2. The ramp rate of the coil current is set slow enough to grant a quasistatic behavior of the hysteresis curve.
3. The cycle of the magnetization is repeated until the resulting B field becomes reproducible.
4. The coils are cooled to provide a stable operation temperature.

Following these rules, the $\vec{B}(I)$ dependence becomes unambiguous down to the noise level (defined e.g. by the quality of the power supply) and it allows usage of simplified non-hysteretic simulation methods. The most commonly used 3D magnetostatics simulation codes in the accelerator community such as CST EMS [19], Opera Tosca [30], COMSOL AC/DC [31] and Ansys Maxwell [32], are based on approaches using the so-called virgin curve[1]. The virgin B-H curve starts at the point of the fully demagnetized state (H=0,B=0) and ends at one of the points of maximal absolute magnetization ($H_{\max}$,$B_{\max}$) or ($-H_{\max}$,$-B_{\max}$). This approach is sufficient for many applications with soft magnetic materials because of their narrow hysteresis curve.

2.3 Beam dynamics

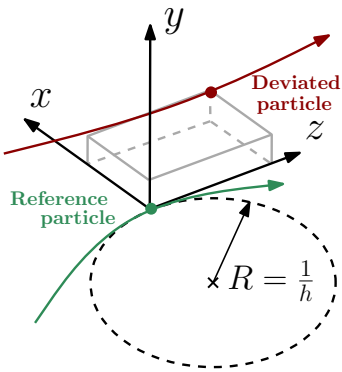

Figure 2.2: Moving beam physics coordinate system. The point $(x, y, z) = (0, 0, 0)$ corresponds to the reference particle. R is the momentary deflection radius and h is the momentary curvature of the reference trajectory.

In particle accelerators, ensembles of moving charged particles are forming beams, which means that their coordinates and momenta are close to each

[1] The transient hysteresis simulation module available e.g. in Opera, is so far impractical for magnetostatic simulations due to much larger computational times.

other. In such cases it is convenient to describe the motion of the particles in a beam using the coordinates relative to one of the particles, namely the reference particle. In Fig. 2.2 a moving curvilinear coordinate system of the reference particle is shown. In the coordinates (x, y, z), the reference particle always stays in the origin, whereas the coordinates of a deviated particle change along its path.

The particle dynamics can be described in terms of state vectors

$$\vec{z} = (z_1, \ ..., \ z_\nu),$$

containing all the values which can change along the motion (momenta, coordinates, energy, mass, spin, etc.), and the independent variable s, which is the path length along the reference trajectory. The changes of a state vector along s is a function of s and of the initial conditions

$$\vec{z}(s) = \mathscr{F}(s, \vec{z}(0)) \tag{2.8}$$

and can be written as a mapping

$$\vec{z}_\mathrm{f} = \mathscr{M}_\mathrm{if} \circ \vec{z}_\mathrm{i}.$$

Here $\mathscr{M}$ stands for the mapping (or map) from the initial plane (index i) to the final plane (index f) and the sign $\circ$ means composition. The initial and final state vectors, which are related by such maps are actually lying in planes which are perpendicular to the reference path. Such maps are origin preserving, indeed, as soon as the reference particle position defines the origin of the curvilinear coordinates, for any s it will stay in the origin. An important property of such maps is that the composition of two maps can again be written as a map

$$\mathscr{M}_{S_2S_3} \circ \mathscr{M}_{S_1S_2} = \mathscr{M}_{S_1S_3} \tag{2.9}$$

with the initial/final planes at $s = S_{1,2,3}$. Particle accelerators can be classified as weakly nonlinear systems, allowing the usage of perturbation methods for the description of particle motion, which helps to reduce the calculation time drastically. In the frame of a perturbation analysis, the state vector $\vec{z}(s) = \mathscr{F}(s, \vec{z}(s_0))$ can be expanded in a Taylor series around the point $s = s_0$.

Truncating this Taylor series at order n results in an n^{th} order transfer map between s_1 and s_0. For a component z_i the expansion can be written as

$$z_i(s_1) = \overbrace{\sum_{k=1}^{\nu} \mathscr{M}^{ik}(s_1) z_k(s_0)}^{1 \text{ order}} + \overbrace{\sum_{k=1}^{\nu}\sum_{l=1}^{\nu} \mathscr{M}^{ikl}(s_1) z_k(s_0) z_l(s_0)}^{2 \text{ order}} + \text{higher orders}, \tag{2.10}$$

where ν is number of entries in z while $\mathscr{M}^{ik}$ and $\mathscr{M}^{ikl}$ are expansion coefficients of first and second order, respectively.

The method of describing the motion of charged particles in electromagnetic fields by means of truncated maps is called *ion-optical approach* because of its similarity to light optics. For systems with very small beam sizes and rather uniform electromagnetic fields, it is sometimes sufficient to account only for the first order of the expansion in Eq. (2.10). In such case the system can be modeled by means of linear algebra, allowing to perform complicated analysis at low computational costs. For example, to study only transversal motion in a horizontal plane, operations with square 2×2 matrices suffice for the analysis of the system. For systems with bigger transversal beam sizes in non-uniform fields, the particles in the beam are exposed to fields that cannot be described with first order approximations anymore. The modeling of such systems requires higher order maps and hence more complicated computations.

Since the beginning of the era of ion optics, a large number of different ion-optical codes (software) was developed. TRANSPORT [33], COSY 5 [34], GICOSY [35], COSY INFINITY [20], MAD [36], SAD [37], and ZGOUBI [38] are only a few of them.

Due to the importance of ring accelerators, where particles can circulate millions of times, many codes are inclined towards preserving symplecticity at the cost of accurate electromagnetic field representation, and are thus restricted to lower orders. In magnetic field based separators, which are normally one-flight systems, the strict symplecticity is not required. But realistic maps, valid in a large aperture range are crucial to achieve a good resolution, especially when rare isotopes are studied. Therefore, for the elaborations in this work, the code COSY INFINITY has been chosen, since it allows high order computation (the order is only limited by the computer/operating system capacity) together with a major development flexibility [39]. Being a script language with a rather comprehensive beam dynamics library [40], it gives users the freedom to create their custom procedures or even add new physics with a little effort. Further in this writing COSY INFINITY will be often mentioned as

COSY, which is not ambiguous, because the earlier versions of this code were not used in this work.

In COSY, the dynamics of particles with constant mass and charge is described by a state vector

$$\vec{z} = \begin{pmatrix} x \\ y \\ a = p_x/p_0 \\ b = p_y/p_0 \\ l = -(t - t_0)v_0\gamma/(1+\gamma) \\ \delta = (E_k - E_{k0})/(E_{k0}) \end{pmatrix}, \tag{2.11}$$

where x and y are the coordinate deviations from the reference particle (as illustrated in Fig. 2.2), a and b are the relative momentum deviations. The index "0" points out the reference particle. E_{k0}, p_0 , v_0, t_0, and γ are the kinetic energy, s-directed momentum, velocity, time of flight and relativistic factor, respectively.

The state vector $\vec{z}$ forms three pairs of canonically conjugate variables ($x - a$, $y - b$ and $l - \delta$). The canonical equations of motion for these variables in curvilinear coordinates are derived in [10] from a full Hamiltonian of a charged particle in an electromagnetic field (see also [41, 42]). The canonical equations of motion for the planar reference trajectory in absence of the electric field can be written as

$$x' = a(1+hx)\frac{p_0}{p_s}, \tag{2.12}$$

$$y' = b(1+hx)\frac{p_0}{p_s}, \tag{2.13}$$

$$l' = -\left((1+hx)\frac{1+\eta}{1+\eta_0}\frac{p_0}{p_s} - 1\right)\frac{\eta_0+1}{\eta_0+2}, \tag{2.14}$$

$$a' = (1+hx)\left(b\frac{B_s}{B\rho_0}\frac{p_0}{p_s} - \frac{B_y}{B\rho_0}\right) + h\frac{p_s}{p_0}, \tag{2.15}$$

$$b' = (1+hx)\left(\frac{B_x}{B\rho_0} - a\frac{B_s}{B\rho_0}\frac{p_0}{p_s}\right), \tag{2.16}$$

$$\text{and} \quad \delta' = 0. \tag{2.17}$$

Here $h = B_y/B\rho$ is the momentary horizontal curvature and $\eta = E_k/E_0$ is the ratio of the kinetic to the rest energy. Eqs. (2.12) - (2.17) are handling only single particle dynamics and do not consider any interactions of the particles between each other.

2.4 Differential Algebraic approach

Differential algebraic (DA) technique is a powerful tool used in numerical computations, especially for nonlinear beam dynamics calculations in accelerator physics [12]. The main idea of the DA approach is to model complicated physical systems on computers with machine precision by using mere arithmetical operations. While the broad introduction and accurate mathematical formalism of the DA approach can be found in [10], here just a brief insight into it will be given. The most important properties of the DA approach will be illustrated with examples.

Structure ${}_nD_\nu$

The elements of the structure ${}_nD_\nu$ are polynomials of order n with a number of variables ν. The coefficients of the monomials building the polynomials are written and stored in a strict order, which can be illustrated by the example of storing the function

$$f(x_1, x_2) = 4 \cdot x_2^2 + 5 \cdot x_1 x_2 + 3x_1 + 8.$$

The DA form of f in ${}_2D_2$ is represented by the array

$$\overset{1}{(8}, \overset{x_1}{3}, \overset{x_2}{0}, \overset{x_1^2}{0}, \overset{x_1x_2}{5}, \overset{x_2^2}{4}).$$

The first element of the array is a constant term, and all the subsequent elements are so called differential terms. The elements in the DA structure are ordered so that the following statement is true:

$$\forall\ \alpha \neq 0 \in \mathbb{R},\ \ \alpha > d_1 > d_2 > ... > d_\nu > d_1^2 > d_1 d_2 > ... > d_\nu^n > 0, \quad (2.18)$$

where d_i are the differential parts of the variables forming ${}_nD_\nu$. The basis of the resulting vector structure has $N(n,\nu)$ elements:

$$N(n,\nu) = \dim {}_nD_\nu = \binom{n+\nu}{\nu} = \frac{(n+\nu)!}{n!\,\nu!}. \tag{2.19}$$

The definition of addition, subtraction, multiplication, as well as inverse multiplication (for elements with non-zero constant part) as operations makes this structure to an algebra. With addition of derivation and antiderivation as operations it becomes a differential algebra. As shown in Fig. 2.3, the operations "+", "—", "·" and "/" on the space of the real analytical functions commute with the operation of the truncation T_n. The operations of derivation and antiderivation do not commute exactly, as soon as the corresponding operations on the ${}_nD_\nu$ space lead to loss of the highest order entries in the DA vector, i.e., maps ${}_nD_\nu$ not onto itself, but rather onto ${}_{n-1}D_\nu$.

Using DA, Taylor expansions up to an arbitrary order of any polynomial or rational function $f(p)$ can be found exactly in any point p_0 where $f(p_0)$ is analytical using the DA arithmetics rules as is illustrated below for the example of ${}_1D_1$. Of practical importance is the DA fixed-point theorem [12], which allows to find solutions of many problems, using a fixed-point formulation, in a finite number of iterations (utmost $n+1$ for the case of ${}_nD_\nu$).

All properties mentioned above make the DA approach to a powerful tool, allowing to solve a great variety of numerical problems in a very elegant manner up to machine precision by means of arithmetical operations.

Structure ${}_1D_1$

In ${}_1D_1$ all vectors are represented by an array (c,d) with constant term c and differential term d. The vectors of type (0,d) are infinitesimal, which means that they are smaller than any vector of type $(c,0)$ with $c>0$. The arithmetic operations on ${}_1D_1$ can be performed using the following rules:

Addition :	$(a_1,a_2)+(b_1,b_2)=(a_1+b_1,a_2+b_2)$
Multiplication :	$(a_1,a_2)\cdot(b_1,b_2)=(a_1b_1,a_1b_2+b_1a_2)$
Multiplicative inversion :	$\dfrac{1}{(a_1,a_2)}=\left(\dfrac{1}{a1},\dfrac{a_2}{a_1^2}\right)$

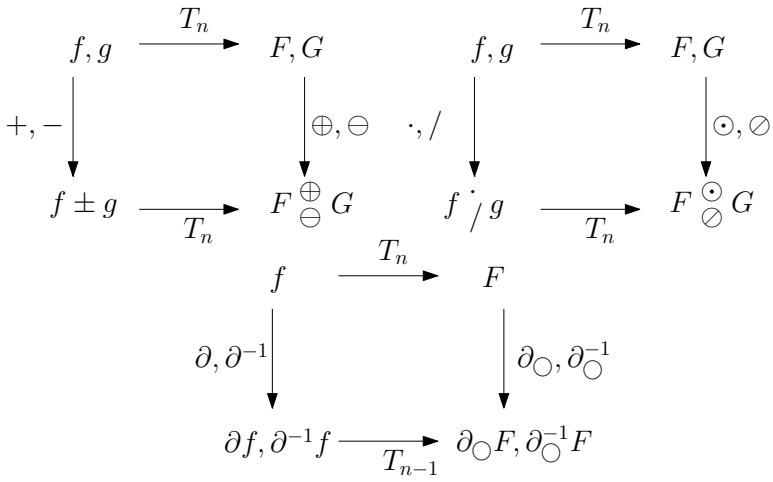

Figure 2.3: Commutation diagram for the operations "+", "—", "·", "/", ∂, and ∂^{-1} on the space of real analytical functions and the truncation operation up to order n, denoted as T_n. The symbols $\oplus$, $\ominus$, $\odot$, $\oslash$, $\partial_{\bigcirc}$, $\partial_{\bigcirc}^{-1}$ stand for the corresponding operation on the differential algebraic space.

Example 1. Let us evaluate the function

$$f(v) = 1/\left(v + \frac{1}{v}\right)$$

and its first derivative for $v = 2$ using DA. For this a DA vector with constant term 2 and a unit differential term $v^{DA} = (2, 1)$ has to be substituted in the DA version of $f(v)$, $f^{\mathrm{DA}}(v^{\mathrm{DA}})$ and $f^{\mathrm{DA}}(2, 1)$ has to be evaluated using the rules of DA arithmetics:

$$f^{\mathrm{DA}}((2,1)) = \frac{1}{(2,1) + \frac{1}{(2,1)}} = \frac{1}{(2,1) + \left(\frac{1}{2}, -\frac{1}{4}\right)} = \frac{1}{\left(\frac{5}{2}, \frac{3}{4}\right)} = \left(\frac{2}{5}, -\frac{3}{25}\right).$$

The differential part of the resulting DA vector is equal to the derivative of $f(v)$ for $v = 2$. Evaluating the function $f(2)$ and $f'_v(2)$ by hand leads to the same answer.

In the same manner it is possible to calculate an exact Taylor expansion up to an arbitrary order for all rational, polynomial functions, roots and any combinations of them. The rules can be extended for evaluation of roots for finite and positive DA-vectors, and for the evaluation of special functions, such as e^x, $\sin(x)$, $\cos(x)$ and $\log(x)$. The corresponding DA expressions can be found in [43] (chapter 8).

2.5 Surface Integration Helmholtz Method

The Surface Integration Helmholtz Method (SIHM), implemented in COSY INFINITY [20], allows to extract the magnetic field vector field together with its Taylor coefficients in an arbitrary point in a source-free 3D volume Ω, starting from its values on the surface $\partial\Omega$ enclosing Ω. A comprehensive explanation and derivation of this method can be found in [16] and [17]. The principle of SIHM is based on the Helmholtz decomposition theorem for finite volumes [44].

Theorem 1. *A general continuous three-vector field that is defined everywhere in a finite volume Ω of a Euclidean three-space and whose tangential and normal components on the bounding closed surface $\partial\Omega$ are given may be uniquely represented by the sum of an irrotational part and a solenoidal part.*

For the magnetic field $\vec{B}$, the Theorem 1 means the satisfaction of the following equation:

$$\vec{B}(\vec{r}) = \vec{\nabla}\varphi(\vec{r}) + \vec{\nabla} \times \vec{A}(\vec{r}), \tag{2.20}$$

where φ and $\vec{A}$ are the scalar and the vector potential, respectively. Utilizing the fact that in a source-free homogeneous region, both potentials satisfy the scalar and vector Laplace equation, respectively, they can be calculated by

$$\varphi(\vec{r}) = \frac{1}{4\pi} \int_{\partial\Omega} \frac{\vec{n}(\vec{r}_s) \cdot \vec{B}(\vec{r}_s)}{|\vec{r} - \vec{r}_s|} ds \quad \text{and} \tag{2.21}$$

$$\vec{A}(\vec{r}) = -\frac{1}{4\pi} \int_{\partial\Omega} \frac{\vec{n}(\vec{r}_s) \times \vec{B}(\vec{r}_s)}{|\vec{r} - \vec{r}_s|} ds. \tag{2.22}$$

Here $\vec{r}_s$ is the vector of the position on $\partial\Omega$, $\vec{r}_v = (x_v, y_v, z_v)$ is the vector of the position inside Ω and $\vec{n}(\vec{r}_s)$ is the normal vector to the surface.

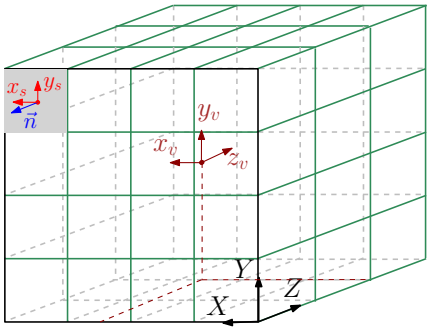

Figure 2.4: Surface, volume and global coordinates for the definition of the SIHM problem. The indices s and v correspond to surface and volume coordinates, respectively. The global coordinates are shown without indices. Each surface element has its own coordinate system.

In the DA framework, to compute the vector and scalar potentials, the integrands in Eq. (2.21) and Eq. (2.22) are expanded in Taylor series in both the surface and the volume variables (using the similar procedure as in Example 1). For computational convenience, the surface $\partial\Omega$ is split into smaller elements on which the input field is defined. The integration on one surface element is performed using the DA antiderivation operation [10]. Summing up the results of the integration along the whole surface and substituting the resulting potentials in Eq. (2.20) results in a DA vector

$$\vec{B}(x_\mathrm{v}, y_\mathrm{v}, z_\mathrm{v}).$$

In Fig. 2.4 an example of the surface, volume and global coordinates used in SIHM is shown. It is important to notice that each surface element (squares in this example) has its own coordinate system.

2.6 Least squares methods for polynomial fitting

This section summarizes the least squares methods (see e.g. [45]), relevant for this work. In this section, matrices are denoted by bold uppercase letters.

The least squares problem setting for a given set of values $(x_\mathrm{i}, y_\mathrm{i})$, where $i \in [1, \ldots, m]$ is to find $f(x)$, such that the sum of squares of errors

$$S = \sum_{i=0}^{m} \varepsilon_\mathrm{i}^2 = \sum_{i=0}^{m} (f(x_\mathrm{i}) - y_\mathrm{i})^2 = \|\vec{\varepsilon}\| \tag{2.23}$$

is minimized.

For a polynomial function

$$f(x) = \sum_{i=0}^{n} C_i x^i, \tag{2.24}$$

the linear system of equations for the least squares problem can be written in matrix form:

$$\begin{bmatrix} 1 & x_1 & x_1^2 & \dots & x_1^n \\ 1 & x_2 & x_2^2 & \dots & x_2^n \\ \vdots & \vdots & \vdots & \ddots & \vdots \\ 1 & x_m & x_m^2 & \dots & x_m^n \end{bmatrix} \cdot \begin{bmatrix} C_0 \\ C_1 \\ C_2 \\ \vdots \\ C_n \end{bmatrix} = \begin{bmatrix} y_1 \\ y_2 \\ \vdots \\ y_m \end{bmatrix} + \begin{bmatrix} \varepsilon_1 \\ \varepsilon_2 \\ \vdots \\ \varepsilon_m \end{bmatrix}, \tag{2.25}$$

or shortly

$$\mathbf{X}\vec{C} = \vec{y} + \vec{\varepsilon}. \tag{2.26}$$

Minimizing S can be done by enforcing the following equation:

$$\frac{d\vec{\varepsilon}}{d\vec{C}} = 0. \tag{2.27}$$

Substituting (2.24) and ε_i from (2.25) into (2.27) results after some arithmetics in the so called normal equations.

$$\mathbf{X}^T\mathbf{X}\vec{C} = \mathbf{X}^T\vec{y}. \tag{2.28}$$

The solution of (2.28) for $\vec{C}$ corresponds to the minimization of S. It should be noted that (2.28) is valid not only for polynomials, but also for any function $f(x)$ which is linear in the coefficients C_i.

The generalization of the method for v variables can be performed easily by ordering the variables and coefficients. Then the polynomial $f(x_1, \dots, x_v)$ can be written as

$$f(x_1, \dots, x_v) = \sum_{i=0}^{n} \sum_{i_1=i}^{0} \sum_{i_2=i-i_1}^{0} \cdots \sum_{i_v=i-i_1-\cdots-i_{v-1}}^{0} C_{i_1,i_2,\dots,i_v} x_1^{i_1} x_2^{i_2} \dots x_v^{i_v} = \\ = C_{0,\dots,0} + C_{1,0,\dots,0} x_1 + \dots + C_{0,\dots,n} x_v^n. \tag{2.29}$$

Sometimes, especially if the number of points is not large enough in comparison to the number of fitting coefficients, the solution of the least squares problem is unstable and leads to strong oscillations of the solution between the points. For equidistantly sampled points these oscillations are known as the Runge phenomenon [46]. To avoid the oscillations it can be helpful to fit not only the function values, but also the derivatives, if they are available. Adding the first order derivatives in system (2.24) leads to additional rows of the form

$$[0, 1, 2x_\mathrm{i}, ..., nx_\mathrm{i}^{n-1}]$$

in the matrix $\mathbf{X}$ and to corresponding values $(dy/dx)|_{x=x_\mathrm{i}}$ in the vectors $\vec{y}$ (the vector $\vec{\varepsilon}$ will double its length in this case).

2.6.1 Constrained least squares

Often it is required to find a fit of a curve which grants strict fulfillment of some constraint conditions. While different solution variants together with proofs can be found in [47] and [48], here only the solution approach based on QR decomposition from [47] (mentioned in [47] as null space method) will be presented. A constrained problem formulation is

$$\begin{aligned} &\text{minimize } \|\mathbf{X}\vec{C} - \vec{y}\| \\ &\text{subject to } \mathbf{D}\vec{C} = \vec{b}, \end{aligned} \tag{2.30}$$

where $\mathbf{D}$ and $\vec{b}$ define the constraints. The normal equations for a constrained problem can be obtained by applying the Lagrange multipliers method [49] to Eq. (2.30), resulting in

$$\begin{bmatrix} \mathbf{X}^T\mathbf{X} & \mathbf{D}^T \\ \mathbf{D} & 0 \end{bmatrix} \cdot \begin{bmatrix} \vec{C} \\ \lambda \end{bmatrix} = \begin{bmatrix} \mathbf{X}^T\vec{y} \\ \vec{b} \end{bmatrix}, \tag{2.31}$$

where λ is any vector satisfying Eq. (2.31). After computing the QR decomposition

$$\mathbf{D}^T = \mathbf{Q} \cdot \begin{bmatrix} \mathbf{R} \\ 0 \end{bmatrix} = \begin{bmatrix} \mathbf{Q}_1, \mathbf{Q}_2 \end{bmatrix} \cdot \begin{bmatrix} \mathbf{R} \\ 0 \end{bmatrix} \tag{2.32}$$

and introducing a new unknown $\vec{z} = \mathbf{Q}^T \vec{C}$, the constraint in (2.30) becomes

$$\mathbf{D}\vec{c} = \mathbf{D}\mathbf{Q}\vec{z} = \begin{bmatrix}\mathbf{R}^T & 0\end{bmatrix} \cdot \vec{z} = \mathbf{R}^T \cdot \vec{z}_1 = \vec{b}, \text{ with } \vec{z} = \begin{bmatrix}\vec{z}_1 \\ \vec{z}_2\end{bmatrix}. \tag{2.33}$$

The general solution of (2.33) is $\vec{z}_1 = (\mathbf{R}^T)^{-1}$ and an arbitrary $\vec{z}_2$. Substituting

$$\mathbf{X} \cdot \mathbf{c} = \mathbf{X}\mathbf{Q}\mathbf{Q}^\mathbf{T}\mathbf{c} = \mathbf{X} \cdot \mathbf{Q}\begin{bmatrix}\vec{z}_1 \\ \vec{z}_2\end{bmatrix} = \mathbf{X} \cdot (\mathbf{Q}_1 \cdot \vec{z}_1 + \mathbf{Q}_2 \cdot \vec{z}_2)$$

in

$$\|\mathbf{X}\vec{C} - \vec{y}\|$$

leads to the unconstrained least squares problem:

$$\text{minimize } \|\mathbf{X} \cdot \mathbf{Q}_2 \cdot \vec{z}_2 - (\vec{y} - \mathbf{X} \cdot \mathbf{Q}_1 \cdot \vec{z}_1)\|. \tag{2.34}$$

The solution of (2.34) can be obtained after the following algorithmic steps:

1. Compute the QR decomposition of $\mathbf{D}^T$: $\mathbf{D}^T = \mathbf{Q} \cdot \begin{bmatrix}\mathbf{R} \\ 0\end{bmatrix} = \begin{bmatrix}\mathbf{Q}_1, \mathbf{Q}_2\end{bmatrix} \cdot \begin{bmatrix}\mathbf{R} \\ 0\end{bmatrix}$,
2. compute $\vec{z}_1$ and $\vec{C}_1 = \mathbf{Q}_1 \cdot \vec{z}_1$,
3. form $\tilde{\mathbf{X}} = \mathbf{X} \cdot \mathbf{Q}_2$ and $\tilde{\vec{y}} = \vec{y} - \mathbf{X} \cdot \vec{C}_1$,
4. solve $\tilde{\mathbf{X}} \cdot \vec{z}_2 \approx \tilde{\vec{y}}$,
5. compute $\vec{C} = \mathbf{Q} \cdot \begin{bmatrix}\vec{z}_1 \\ \vec{z}_2\end{bmatrix} = \vec{C}_1 + \mathbf{Q}_2 \cdot \vec{z}_2$.

2.6.2 Piecewise C^2-smooth polynomial approximation

Finding a piecewise polynomial approximation to a curve satisfying C^2-smoothness in the whole range of approximation can be formulated as constrained least squares problem (2.30). In a preprocessing step, the whole data set $(\vec{x}, \vec{y})$, containing n points, must be split into m pieces with lengths $[k_1, k_2, \ldots, k_m]$, so that

$$\sum_{i=1}^{m} k_i = n,$$

in which the data are interpolated with the polynomials

$$ {}^{j}y_{\mathrm{i}} = \sum_{l=0}^{n} C_{j,l}\ {}^{j}x_{\mathrm{i}}^{l}, $$

where the indices j and i mean the index of the piece and the index of the point in the piece, respectively. The expression $(\mathbf{X}\vec{c} - \vec{y})$ for the whole set $(x_{\mathrm{i}}, y_{\mathrm{i}})$ can then be written as

$$ \mathbf{X}\vec{c} - \vec{y} = \begin{bmatrix} 1 & {}^{1}x_1 & {}^{1}x_1^2 & \dots & {}^{1}x_1^n \\ \vdots & \vdots & \vdots & \ddots & \vdots \\ 1 & {}^{1}x_{k_1} & {}^{1}x_{k_1}^2 & \dots & {}^{1}x_{k_1}^n \\ \vdots & \vdots & \vdots & \ddots & \vdots \\ 1 & {}^{m}x_1 & {}^{m}x_1^2 & \dots & {}^{m}x_1^n \\ \vdots & \vdots & \vdots & \ddots & \vdots \\ 1 & {}^{m}x_{k_m} & {}^{m}x_{k_m}^2 & \dots & {}^{m}x_{k_m}^n \end{bmatrix} \cdot \begin{bmatrix} {}^{1}C_1 \\ \vdots \\ {}^{1}C_n \\ \vdots \\ {}^{m}C_1 \\ \vdots \\ {}^{m}C_n \end{bmatrix} - \begin{bmatrix} {}^{1}y_1 \\ \vdots \\ {}^{1}y_{k_1} \\ \vdots \\ {}^{m}y_1 \\ \vdots \\ {}^{m}y_{k_m} \end{bmatrix}. \tag{2.35} $$

The constraint conditions for the connection points $x_{C,i}$ can then be written as

$$ \begin{aligned} f_i(x_{C,i}) - f_{i+1}(x_{C,i}) &= 0, \\ f_i'(x_{C,i}) - f_{i+1}'(x_{C,i}) &= 0, \\ f_i''(x_{C,i}) - f_{i+1}''(x_{C,i}) &= 0, \end{aligned} \tag{2.36} $$

where $i \in \{1, m-1\}$. The condition matrix written for all points has a block-diagonal form

$$ \begin{bmatrix} \mathbf{D}_1^{left} & \mathbf{D}_1^{right} & 0 & & & \\ 0 & \mathbf{D}_2^{left} & \mathbf{D}_2^{right} & 0 & & \\ & & & \ddots & & 0 \\ & & & 0 & \mathbf{D}_{m-1}^{left} & \mathbf{D}_{m-1}^{right} \end{bmatrix}, \tag{2.37} $$

with blocks

$$\mathbf{D}_{\mathrm{i}}^{\mathbf{left}} = \begin{bmatrix} 1 & x_{C,i} & x_{C,i}^2 & \dots & x_{C,i}^n \\ 0 & 1 & 2x_{C,i} & \dots & nx_{C,i}^{n-1} \\ 0 & 0 & 2 & \dots & (n-1)nx_{C,i}^{n-2} \end{bmatrix},$$
$$\text{and } \mathbf{D}_{\mathbf{i}}^{\mathbf{right}} = \begin{bmatrix} -1 & -x_{C,i} & -x_{C,i}^2 & \dots & -x_{C,i}^n \\ 0 & -1 & -2x_{C,i} & \dots & -nx_{C,i}^{n-i} \\ 0 & 0 & -2 & \dots & -(n-1)nx_{C,i}^{n-2}. \end{bmatrix}. \tag{2.38}$$

The solution of the resulting constrained least squares problem is straightforward with the method described in Sec. 2.6.1.

3 Magnetic field measurements and simulations

In this chapter, aspects of magnetic field simulations and measurements are illuminated using the example of the Super-FRS normal conducting (NC) 11° dipole magnet (see 3.1) built and measured at the Budker Institute of Nuclear Physics (BINP). Further in this chapter the considered Super-FRS dipole magnet will be named simply ”dipole” or ”magnet”. The simulated magnetic field is compared with the measurement data from [50]. This magnet was chosen because up to at least end of 2018 it was the only successfully built and measured prototype which is going to be installed in the Super-FRS. Nevertheless, the elaborations in this work are general and can be applied to any other large-aperture DC magnet as well. The text in this chapter is partially adopted from the author's publications [51] and [52].

3.1 NC 11° dipole magnet of the Super-FRS

The object of the following discussions is the NC 11° dipole magnet [18] of the first stage of the Super-FRS shown in Fig. 3.1. The iron yoke is colored red and both coils together with the water-cooled radiators are potted in tin-lead solder, observable in the photo. The main parameters of the dipole are listed in Tab. 3.1 [53].

For the magnetic simulations of the dipole the *B-H* hysteresis curve together with the virgin curve were measured using a permeameter [54] at GSI. The result is depicted in Fig. 3.2.

The dipole will be powered by a unipolar current source. For this reason, during the current ramping, the physical magnetization of the yoke will not proceed along the outer hysteresis branches but rather along some other sub-branches which start from the remanent field $\vec{B}_r(\vec{r})$. Such branches can lay between the upper hysteresis branch and the virgin curve in Fig. 3.2. Since used magnetostatic codes require usage of the virgin curve, a considerable difference between the magnetic measurements and simulations is expected for low currents.

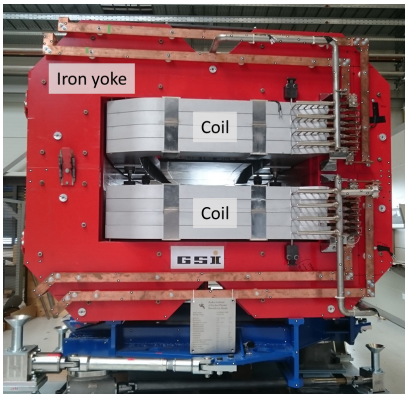

Figure 3.1: Photo of the prototype of the normal conducting 11° Super-FRS dipole magnet with a design bending radius $R_0 = 12.5$ m.

Table 3.1: Parameter list of the Super-FRS NC 11° dipole magnet. Data from [53].

Deflection radius R_0	12.5 m
Deflection angle θ_0	11°
Main field value	0.16 to 1.6 T
Total number of coil turns	384
Coil current	60 to 650 A
Vertical pole gap	180 mm
Usable horizontal aperture	±600 mm
Usable vertical aperture	±70 mm
Horizontal good field region	±190 mm
Vertical good field region	±70 mm
Overall yoke width	2.5 m
Overall magnet height	1.98 m
Overall magnet length	2.9 m

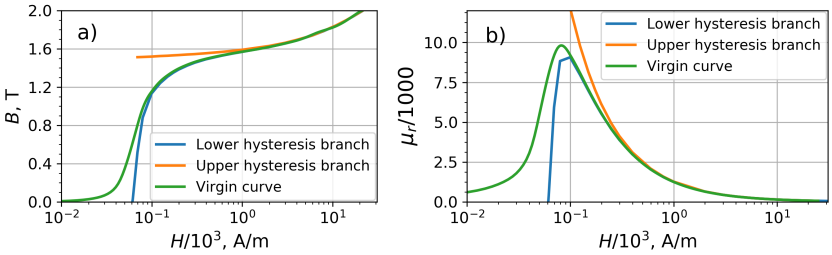

Figure 3.2: Measured magnetization curves of the yoke steel **a)** and the corresponding relative permeability μ_r values **b)** dependent on the magnetic field strength H.

3.2 Simulations in CST EM Studio

For the magnetostatic simulations a 3D model of the magnet in Fig. 3.3 has been created in Autodesk Inventor [55] starting from the technical drawings available at GSI. The origin of the magnet's right-handed coordinate system is placed in a cross-section of its three symmetry planes. The coordinates X, Y and Z correspond to horizontal transversal, vertical and horizontal longitudinal directions, respectively, as depicted in Fig. 3.3.

All the calculations were performed using the third order FEM solver with a tetrahedral mesh and third order finite elements up to a residual of $1 \cdot 10^{-6}$ in CST EM Studio version 2017. The model has been split into subblocks. In each subblock the meshsize was set to $w_{\text{subblock}} \cdot M_{\text{global}}$ with individually chosen weights w_{subblock} and a common factor M_{global}. M_{global} was optimized for reducing the calculation time while preserving accuracy. The resulting mesh shown in Fig. 3.4 is fine in the region of interest and is getting coarser towards the borders of the simulation model.

The symmetry allowed to reduce the size of the actually solved problem to a quarter of the initial model. The coordinates of this quarter are: $X \in [X_{\text{min}} < 0, X_{\text{max}} > 0]$, $Y \in [0, Y_{\text{max}} > 0]$, $Z \in [0, Z_{\text{max}} > 0]$. The total number of tetrahedra in this quarter was about 3.3 million. The boundary conditions were set so that only a perfect dipole field could exist on the borders, i.e., the normal component of the magnetic flux density B_n was forced to zero in the planes X_{min}, X_{max} and Z_{max} and the tangential component of the magnetic field strength H_t was forced to zero in the plane Y_{max}. These conditions are an idealization of the reality and too close boundaries significantly affect the solution. Considering an additional 12 m air/vacuum background space at each side of the simulation model was sufficient for obtaining a convergence of the resulting B-field up to 10^{-6} relatively to the field maximum.

The magnetic field was calculated for an equidistant set of coil currents I from 50 A to 650 A with a step of 25 A as well as for I values of 40, 320, 640 and 740 A for comparison with the measurements performed in 2010 by Budker Institute of Nuclear Physics [50].

3.3 Comparison of the simulated and measured magnetic field

An important property of a magnet is its integral excitation curve (IEC), which is the current dependence of the integral of the magnetic flux density along

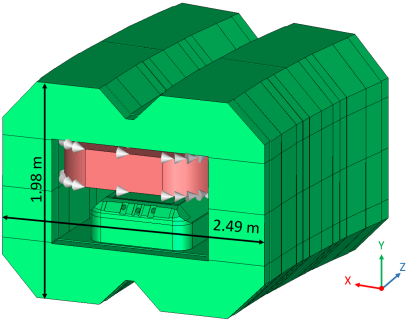

Figure 3.3: 3D CST model of the dipole. Only the upper coil is shown to allow a view on the lower pole.

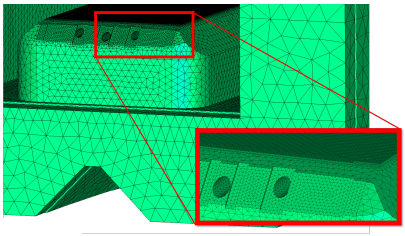

Figure 3.4: Zoomed mesh view of the dipole.

the reference path or along a straight path, parallel to the longitudinal axis[1]. The measured and simulated IEC are shown in Fig. 3.5 **a)** and appear nearly identical. Only after the normalization to I the expected deviation between the simulated and the measured data is visible as depicted in Fig. 3.5 **b)**. The difference is maximal ($\approx$ 0.8%) for $I = 40\,\mathrm{A}$ and is significantly lower for higher currents. The slight shape deviation of the curves originates mainly from the difference in the real and simulated magnetization processes.

The distribution of the B-field along the Z axis for different I values is depicted in Fig. 3.6 **a)**. The relative difference between the measured B_m and simulated B_s field in Fig. 3.6 **b)** in the main field region (-80 cm to 80 cm) originates mainly from the absence of the remanence in the simulations. The non-uniformity of the relative difference along the Z axis can be explained by the different magnetization curves and the unknown inhomogeneity of the magnetic properties of the yoke of the real dipole.

In principle, the relative difference of the measured and simulated field $(B_s - B_m)/B_0$ for $B_0 = 0.1\,\mathrm{T}$ can be estimated analytically. In this estimate the magnetization is described by the magnetic permeability only, i.e., without the introduction of the concept of surface currents. Although such description of the magnetization cannot be used to calculate the magnetic field for $I = 0$,

[1] If the integration is performed along the reference path, the integral of the magnetic flux density is proportional to the deflecting angle θ_0. In case of a straight integration path, its X-coordinate is chosen so that for some current value the integral field value equals $\theta_0 B\rho$. Then, the integral of the magnetic flux density is also roughly proportional to θ_0.

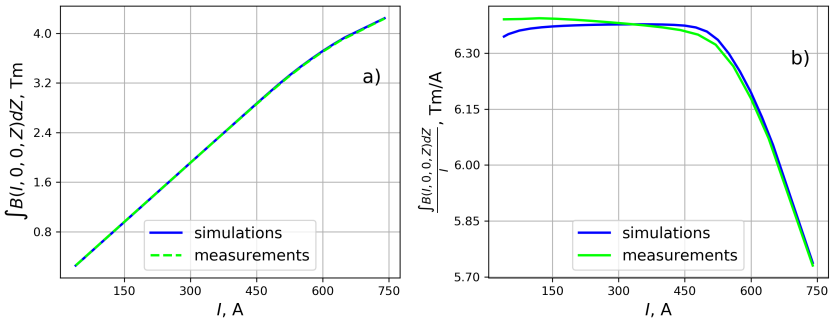

Figure 3.5: Integral excitation curve (IEC) $\int B_Y(0,0,Z,I)dZ$ **a)** and normalized IEC $\int B_Y(0,0,Z,I)dZ/I$ **b)** derived from simulations and measurements.

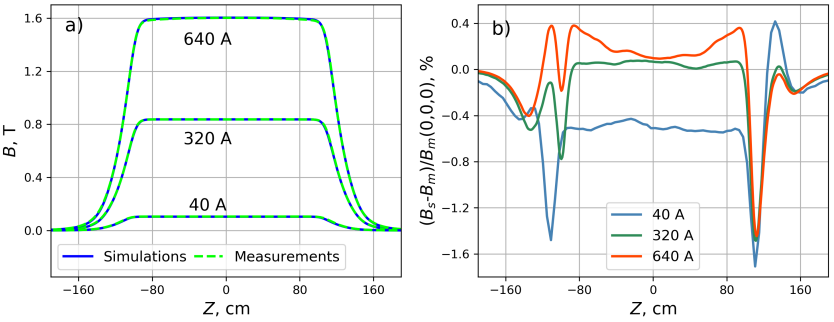

Figure 3.6: Measured B_m and simulated B_s magnetic field along the Z axis **a)** and relative error $(B_m - B_s)/B_m(0,0,0)$ **b)**.

it still allows an estimation of the difference in the main field originating from different magnetization curves. For $H = 0$, B has a non-zero value and hence $\mu_r = \infty$. Whereas in case of the virgin curve in Fig. 3.2, the value $B_0 = 0.1\,\mathrm{T}$ corresponds to $H = 35\,\mathrm{A/m}$ and $\mu_r = 2273$, for the actual magnetization sub-branches the $H(B_0 = 0.1\mathrm{T})$ can be considerably smaller and $\mu_r(B_0 = 0.1\mathrm{T})$ larger. Assuming that H is constant in the yoke, $B{=}B_0$ is constant in both the yoke and the aperture, and the length of the magnetic path in the iron is $L_{\mathrm{yoke}} = 3\,\mathrm{m}$, B_0 can be estimated using Eq. (2.6):

$$B_0 \approx \mu_0(nI - \int_{\mathrm{yoke}} \vec{H} \cdot d\vec{l})/h \approx \mu_0(nI - H \cdot L_{\mathrm{yoke}})/h = \mu_0(nI - \frac{B_0}{\mu_0\mu_r} \cdot L_{\mathrm{yoke}})/h,$$

where h is the aperture height. Hence, for $(B_s - B_m)/B_0$ it follows

$$(B_s - B_m)/B_0 \approx (\frac{1}{\mu_{r,1}} - \frac{1}{\mu_{r,2}}) \cdot \frac{L_{\mathrm{yoke}}}{h}.$$

In the limit of $H(B_0 = 0.1\ \mathrm{T}) = 0$ and $\mu_r = \infty$, a difference in B_0 of 0.69% can be expected. To provide a difference of 0.5%, occurring for 40 A in Fig. 3.6 **b)**, $\mu_r = 8112$ is required for $B = 0.1\,\mathrm{T}$, which corresponds to $H = 9.8\,\mathrm{A/m}$. For this H, the μ_r point is located between the upper hysteresis branch and the virgin curve in Fig. 3.2, as it can be expected. This estimate was crosschecked by 3D simulation of the same model with a modified $B-H$ curve. The idea of the modification was to make the curve steeper in the beginning, so that for $B_0 \approx 0.1\,\mathrm{T}$ $H9.8\,\mathrm{A/m}$ was satisfied. The modified curve also started in point (0,0) and was identical to the virgin curve for $H > 100\,\mathrm{A/m}$. The simulated relative difference in B_0 between the original and modified virgin curves was 0.68% for $I = 40\,\mathrm{A}$ which is in a good agreement with the analytical estimate. Although here no further investigation with the modification of the virgin curve was done, this approach could be useful for achieving a better agreement between the measurements and simulations of unipolar magnets via optimization of the form of the virgin curve at low H values.

Despite the deviations in the longitudinal B-field distributions, the simulated transversal field distributions for 320 A and 640 A are in good agreement with the measurements as shown in Fig. 3.7. The relative offset is in both cases less than $1.1 \cdot 10^{-3}$ and comes from the difference between the simulated and actual magnetization processes as discussed above. The ripples observable in measured data are spread along the whole Z-axis and correspond to a systematic measurement error, originating from the measurement setup. The array of

16 Hall probes with the total width of 16 cm was moved four times to cover the width of 64 cm. The systematic error introduced by the lack of cross-calibration between the probes can be demonstrated by plotting the difference between the measured and simulated field in the main field region as shown in Fig. 3.8. The horizontal period of repeating of the stripe patch is exactly 16 cm.

After the removal of the systematic error from Fig. 3.7 **b)** (dark green line) the measured and simulated field distributions along the X-axis in the middle of the magnet have a similar form. For the distribution measured for 320 A the ripples are smaller so that it is easy to see that the measured and simulated distributions are also in a good agreement.

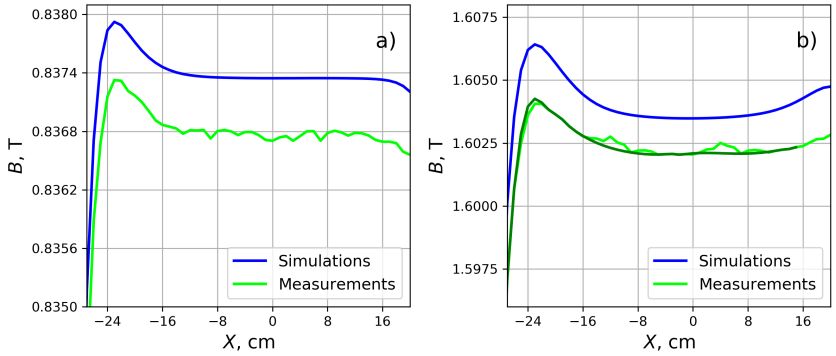

Figure 3.7: Measured and simulated magnetic field along the X axis for $Z=0$ for coil currents of 320 A **a)** and 640 A **b)**. The ripples in the measured data correspond to a systematic measurement error. The dark-green line in **b)** is a result of removing the ripples from the measurement data.

3.4 Saturation effects in the simulated magnetic field

As was mentioned before, magnetic saturation leads to a change of the magnetic field distribution in the yoke. In Fig. 3.9 the distribution of μ_r in one quarter of the yoke cross-section in $Z = 0$ is shown for three different currents. For $I = 50$ A (Fig. 3.9 **a)**) the average H value in the yoke is less than 85 A/m where the maximum of the relative permeability $\mu_{r,max}$ is located (see Fig. 3.2 **b)**). In this case the higher-magnetized inner part of the yoke has

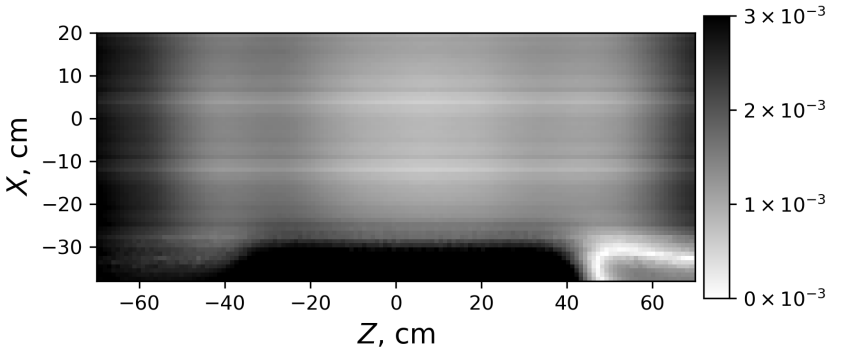

Figure 3.8: Absolute relative difference between the measured and simulated magnetic field for a coil current of 640 A. The horizontal stripes correspond to the systematic error introduced by the measurement setup.

larger μ_r values. For $I = 425$ A (Fig. 3.9 **b)**) the mean magnetization corresponds roughly to $\mu_{r,max}$ and the highest μ_r values are in the inner part of the yoke. Whereas the inner yoke-air interface corresponds to $H > H(\mu_{r,max})$, the outer yoke-air interface has lower μ_r values because of lower H values. For $I = 600$ A (Fig. 3.9 **c)**), the areas with the lowest H have maximal μ_r values, whereas the pole is significantly saturated, revealing a μ_r of more than 10 times less than its maximal value. The changes in the magnetic field distribution due to saturation are mostly located in the area near to the pole ends, where the H values are the highest.

In Fig. 3.10 $B_Y/B_Y(0,0,0)$ is shown along Z for $X = Y = 0$ **a)** and along X for $Y = Z = 0$ **b)**. In **a)** the most significant effect is the decreasing slope of the magnetic field fringes for increasing I values, indeed, for $Z = -80$ cm the magnetic field at $I = 650$ A is 0.6% lower than it is at $I = 50$ to 375 A.

The transversal distribution of B_Y in Fig. 3.10 **b)** reveals a deviation at the aperture sides. For currents below 500 A the deviation is insignificant, while above 500 A it leads to an increase of the peak at about −22 cm and the appearance of another peak around 20 cm.

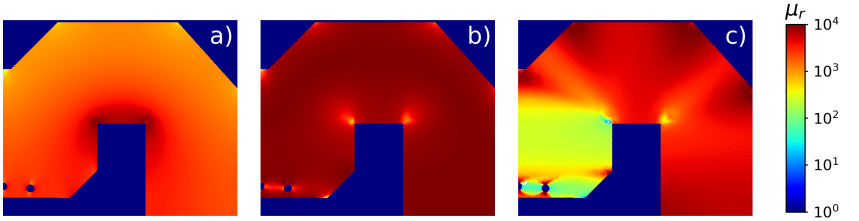

Figure 3.9: Relative permeability μ_r distribution in the quarter of the dipole yoke section in plane $Z = 0$ for coil currents $I = 50\,\text{A}$ **a)**, $I = 425\,\text{A}$ **b)** and $I = 600\,\text{A}$ **c)**.

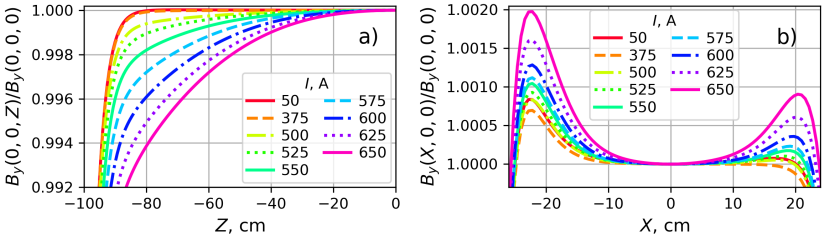

Figure 3.10: B_Y normalized to its value in point $(X, Y, Z) = (0, 0, 0)$ for different currents along Z for $X = Y = 0$ **a)** and along X for $Y = Z = 0$ **b)**.

In the plane $Y = 0$ the change of the $B_Y(I)$ distribution can be described by the function

$$f(I,X,Z) = B_Y(I,X,0,Z)/B_Y(I,0,0,0) - B_Y(50\text{ A},X,0,Z)/B_Y(50\text{ A},0,0,0).$$

The function $f(I,X,Z)$ is plotted in Fig 3.11 for several currents. For the currents below 400 A the relative deformation of the field is very small (less than 10^{-4}). For 650 A, the dark blue areas around $Z = -100$ cm and $Z = 100$ cm correspond to the decreasing slope of the magnetic field fringes in Fig. 3.10 **a)**. The light red areas around $X = -20$ cm and $X = 22$ cm correspond to the changes of the shape in Fig. 3.10 **b)**. The absolute total deviation of the magnetic field distribution is of the order of 10^{-3}, which presumably cannot be neglected in the Super-FRS ion-optical model.

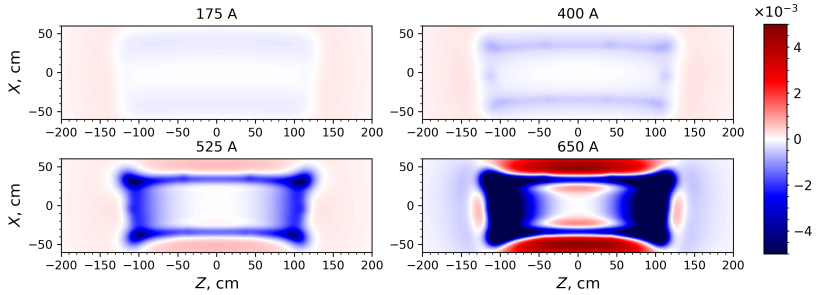

Figure 3.11: Relative change of the normalized $B_Y(I)$ distribution with respect to the normalized $B_Y(50\,\text{A})$ distribution in the plane $Y = 0$ for different currents.

4 Processing of the magnetic field: from raw data to high-order polynomials

For the further ion-optical studies it is important to have a functional dependence of the magnetic field on the coordinates and excitation currents. The main aim of the processing of the magnetic data in this chapter was to develop a method to obtain smooth polynomial functions (DA-vectors), which accurately represents the B-field and satisfy the Laplace equation. The method is based on the SIHM and the least squares approximation described in Secs. 2.5 and 2.6, respectively. The benchmarking and robustness testing of the SIHM were carried out for an analytical magnetic model. Subsequently, the method was adapted for flat volumes and applied to the Super-FRS preseparator dipole magnet.

4.1 Testing the SIHM using an analytical magnetic model

To utilize the SIHM efficiently it is required to know its optimal parameters for a given problem. These parameters are the size of the surface elements, the type of the surface approximation and the order of the DA vectors. In order to exclude an influence of errors in the input field an analytical model is used for the benchmarking. The model used in this work is based on the magnetic field of two current-carrying loops of infinitely thin wire schematically shown in Fig. 4.1. Each loop is a symmetric trapezoid with a height of 1.6 m and a basis length of 2.2 m. The extensions of the lateral sides of the trapezoid are enclosing an angle of 9.75°. Both trapezoids have identical horizontal coordinates and are arranged in parallel at a distance of 1.2 m in vertical (Y) direction. Each loop carries a current I of 2.1 MA. This current is required to produce $B_0 \approx 1.6$ T, the design value of the Super-FRS dipoles for $B\rho = 20$ Tm.

The magnetic field of the wire loops can be calculated using the Biot-Savart law

$$\vec{B}(\vec{r}) = \frac{\mu_0}{4\pi} \int_C I d\vec{l} \times \frac{\vec{r} - \vec{r}'}{|\vec{r} - \vec{r}'|^3}, \tag{4.1}$$

where $\vec{r}'$ is the position of an infinitely small piece of wire $d\vec{l}$ and C is the integration path going along both loops. The arrangement of the wires is chosen so that it resembles the arrangement of the coils of a Super-FRS main separator dipole with a deflecting angle of 9.75° and deflecting radius of 12.5 m. The resulting magnetic field is non-uniform and has the same symmetry as the field of a conventional sector dipole.

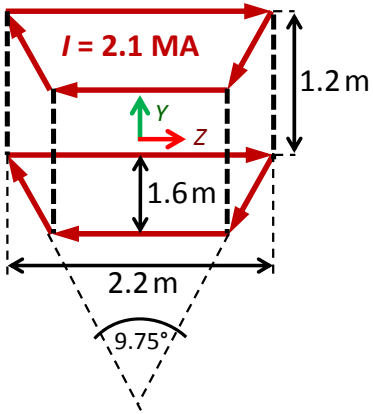

Figure 4.1: Scheme of the analytical model of a thin wire magnet. The red arrows show the current direction. The origin of the right-handed coordinate system is placed in the center of the wire arrangement.

The values of the magnetic field and its derivatives were obtained in COSY using the stable numerical algorithm described in [56], which is suitable to compute the DA vectors of the magnetic field of straight infinitely thin wires. The distribution of the magnetic field in the plane $Y = 0$ is shown in Fig. 4.2.

4.1.1 Benchmarking

As an input for the SIHM the field values (B_X, B_Y, B_Z) were given on a surface of a cuboid $\mathscr{D} = \{X \in [X_{\min}, X_{\max}]$ m, $Y \in [Y_{\min}, Y_{\max}]$ m, $Z \in [Z_{\min}, Z_{\max}]$ m$\} = \{X \in [-0.6, 0.6]$ m, $Y \in [-0.08, 0.08]$ m, $Z \in [-2.2, 2.2]$ m$\}$. On each of the surface faces the input points were forming a quadratic mesh with a grid

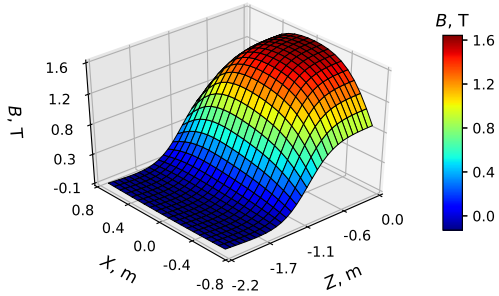

Figure 4.2: Computed magnetic field distribution in the plane $Y = 0$, produced by the wire loops shown in Fig. 4.1. Only a half of a symmetric field distribution is shown.

constant d. The constant d was defined so that each corner of the cuboid coincides with a mesh point. Subsequently, the surface faces were split into sets of square surface elements. Each surface element was as large as an area on the cuboid, covered by an array of 3×3 input points as illustrated in Fig. 4.3. Since the SIHM procedure requires the knowledge of the functional distribution of the magnetic field on the surface elements, a functional approximation of the discrete input data was necessary. Two different approximation methods were used: quadratic polynomial approximation and Gaussian approximation. After the approximation the initial field data is represented by a set of analytical functions on the surface elements. The integration and differentiation in the SIHM equations (2.20)-(2.22) is performed analytically using the DA techniques. It should be noted that the integration over the surface, as well as the differentiation in the DA framework leads to a loss of information of the highest order. The SIHM algorithm contains both integration and differentiation, which leads to a loss of two orders in the resulting B-field DA vectors.

For quadratic approximation of $B_{X,Y,Z}$ on each surface element, 9 input points were used. The approximation was performed on each surface element separately using a least squares fit of the function

$$\begin{aligned} B_i(\xi,\eta) =& c_{00} + c_{10}(\xi-\xi_c) + c_{01}(\eta-\eta_c) + \\ &+ c_{11}(\xi-\xi_c)(\eta-\eta_c) + c_{20}(\xi-\xi_c)^2 + c_{02}(\eta-\eta_c)^2, \end{aligned}$$

where $c_{00},\ldots,c_{02}$ are the fitting coefficients, $i \in \{X,Y,Z\}$, and (ξ_c,η_c) is the center of the element. (ξ,η) is a vector in the local coordinate system of each cuboid face coinciding with the global coordinate pairs (X,Y), (X,Z), (Y,Z). The origin of the local coordinate system is located in the center of the corresponding cuboid face.

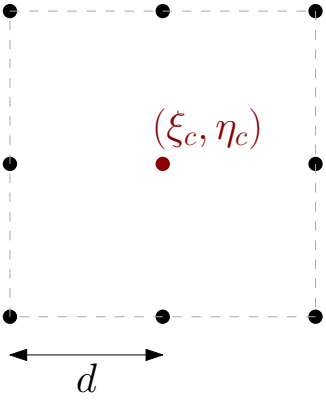

Figure 4.3: Surface element with center (ξ_c,η_c) defined by a 3×3 array of input points in a quadratic grid with constant d.

Gaussian approximation is based on a representation of the magnetic field by a sum of 2D Gaussian functions

$$B_i(\xi,\eta) = \sum_{i_\xi}\sum_{i_\eta} B_i(i_\xi, i_\eta)\frac{1}{\pi S^2}\exp\left(-\left(\frac{\xi-\xi_{i_\xi}}{Sd}\right)^2-\left(\frac{\eta-\eta_{i_\eta}}{Sd}\right)^2\right),$$

centered in the input points. Here ξ_{i_ξ} and η_{i_η} are the coordinates of the point on the grid with indices (i_ξ, i_η) and S is a parameter corresponding to the width of the Gaussian functions. The summation is performed over $8\cdot S$ points (rounded down) in both dimensions, which might cause a lack of accuracy for the edge elements. DA Gaussian approximation is available in COSY as a part of the MF procedure [40].

In Fig. 4.4 the relative error $\Delta B/B$ of the SIHM-generated field depending on the density of the surface elements N_s is compared for quadratic and Gaussian surface approximation as well as for constant approximation. For constant approximation the field on each surface element was set to $\vec{B}(\xi_c,\eta_c)$. In all cases 4^{th} order DA computation was used, resulting in 2^{nd} order output DA vectors.

For the considered configuration quadratic approximation yields an up to 4 orders of magnitude smaller $\Delta B/B$ than the other methods. Apparently Gaussian approximation is not working well for the used problem configuration and even a constant value surface approximation provides a better result. This might be due to the relatively small number of input points per surface element

as well as the lack of information beyond the borders of the cuboid faces. For all approximation methods the error decreases rapidly with N_s and reveals a saturation above 200 elements/m leading to an accuracy of better than 10^{-10} for quadratic approximation. For the best accuracy and moderate computation times the quadratic approximation method and $N_s = 125$ were used in further computations.

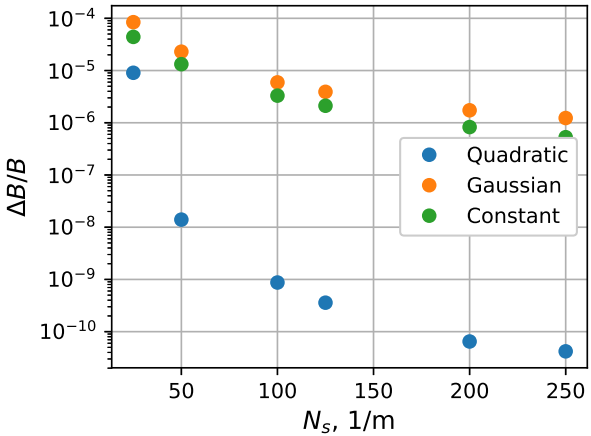

Figure 4.4: Semi-log plot of the relative error for different surface approximation methods of the SIHM-generated magnetic field of the wire loops in Fig. 4.1 versus the number of surface elements per meter N_s. The 4$^{\text{th}}$ order DA computation was used. The error is evaluated in point (0,0,0).

In Fig. 4.5 the dependence of the relative error on the computation order is shown for the magnetic field value and its derivatives $B'_X := dB/dX$, $B'_Z := dB/dZ$ and $B''_{XZ} := d^2B/dX/dZ$ in point (0,0,-1). The field values as well as the shown derivatives converge rapidly with increasing order. The errors in the derivatives are larger than the errors in the magnetic field. Nevertheless, sufficiently close to the expansion point the contribution of the derivatives to the B-field is decreasing exponentially with their order.

Fig. 4.6 shows the relative error of the B_Y component evaluated from polynomials of different orders for the planes $Y = 0$ and $Y = 0.06$ (75% of Y_{max}). For low orders the magnetic field is accurate only in the expansion point and a small region in its proximity. This region grows when increasing the order of the polynomials up to the 13$^{\text{th}}$. A further increase of the order leads to

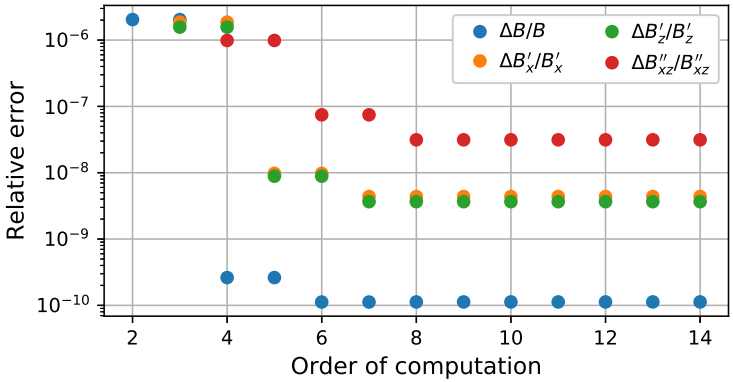

Figure 4.5: Relative error of the SIHM output with respect to the analytic magnetic field in point (0,0,-1) and its derivatives B'_X, B'_Z, and B''_{XZ} against the computation order.

a shrinking of the area where approximated field is accurate. For 20$^{\text{th}}$ order the border of the accurate approximation area is rather sharp (within 6 cm the relative error grows from 10^{-9} to 10^{-2}).

The observed behaviour of the SIHM output polynomials originates from the algorithm. More precisely, the radius of convergence of the Taylor expansion coincides with the radius of holomorphy of the expanded function and cannot exceed the distance from the expansion point to the nearest singularity [57]. From Eqs. (2.21) and (2.22) it can be seen that the nearest singularity is situated on the closest surface element. Although the area of an accurate approximation for the 20$^{\text{th}}$ order in Fig. 4.6 is square-shaped and is larger than the distance to the nearest surface element of 0.08 m, it is expected that it will shrink down to a round area with the radius of 0.08 m when further increasing the order. Since $|\vec{r} - \vec{r}_s|$ is smaller than the horizontal area of interest only for a small fraction of the surface elements, the area of accurate approximation does not shrink very fast.

The fact that in Fig. 4.6 for intermediate orders (e.g. 13$^{\text{th}}$) the field is represented very accurately in a larger region than a sphere with a radius of 0.08 m can be explained by the rather simple shape of its distribution. This behaviour cannot be expected for a magnetic field distribution of the Super-FRS dipoles. Indeed, in Fig. 4.7 the relative error of the SIHM output Taylor polynomials is

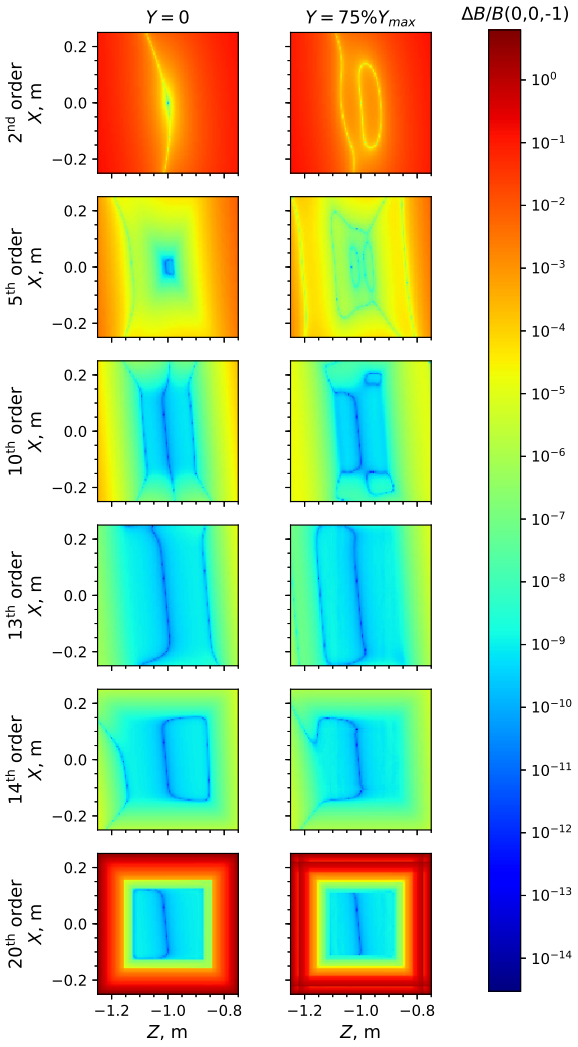

Figure 4.6: Relative error $\Delta B/B(0,0,-1)$ of SIHM output polynomials of various orders with respect to an analytical magnetic field. The error was evaluated in the planes $Y = 0$ and $Y = 0.06$ (75% of $Y_{\max}$). In each plot the expansion point $(0,0,-1)$ was used to evaluate the field.

shown for the magnetic field of the Super-FRS dipole. Here the area of the accurate polynomial field representation is smaller and the error on the borders of the plot is much higher for the 13th and 20th orders. This confirms that the SIHM has its limitation for relatively flat volumes of interest due to the limited radius of holomorphy of the integrands used therein.

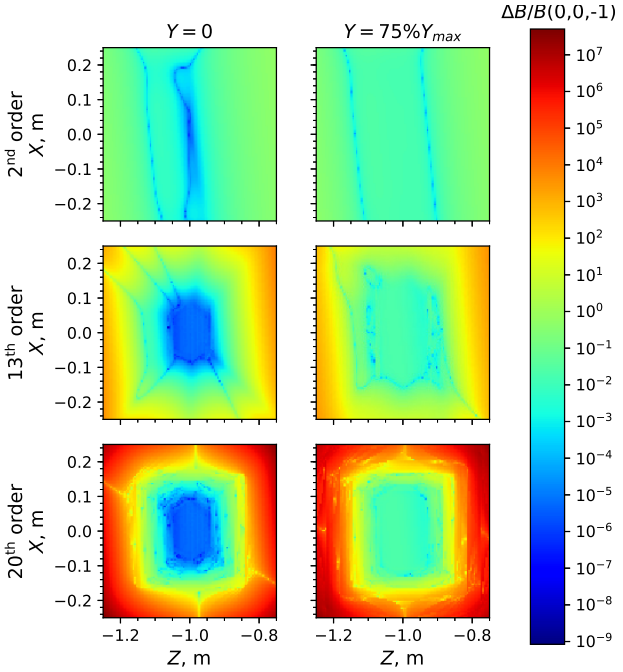

Figure 4.7: Relative error $\Delta B/B(0,0-1)$ of the SIHM output polynomial for the Super-FRS dipole magnet, centered in expansion point (0,0,-1). The error of the polynomials of different orders has been evaluated in the planes $Y = 0$ and $Y = 0.06$ (75% of Y_{max}). The FEM-simulated magnetic field is used as a reference.

4.1.2 Robustness study

Except for analytical cases, the magnetic field data always contain errors related to the measurement or simulation procedure. To estimate the robustness of the SIHM against the magnetic field error, normally distributed random errors were added to the analytical input field values. To quantify the input error, the full width of half maximum (FWHM) of its distribution was used. For each FWHM 1000 samples were calculated in order to determine the statistical properties of the output error distributions. In Fig. 4.8 the FWHM, root mean square RMS and maximum of the resulting error distributions are shown for the magnetic field and its derivatives in point $(0, 0, -1)$. The abscissa of each subplot corresponds to the FWHM of the input error distribution. 4^{th} order of DA computation was used resulting in the 2^{nd} order output polynomials.

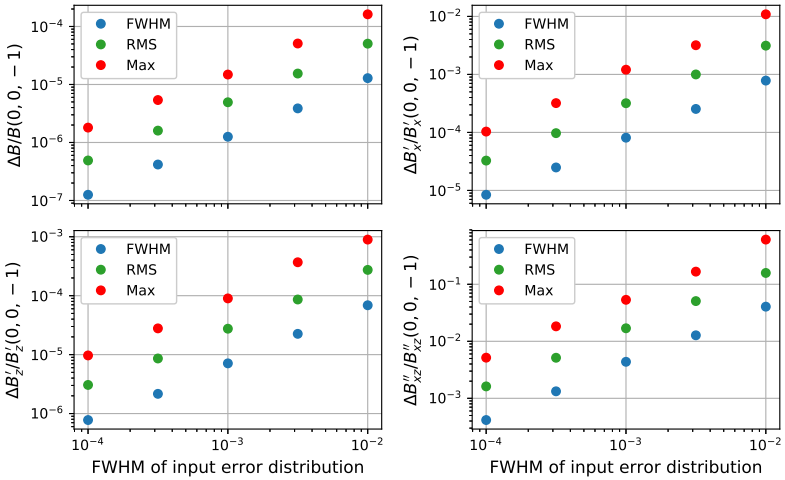

Figure 4.8: Relative errors of the SIHM-computed magnetic field and its derivatives in x, z, and xz directions depending on the FWHM of the input Gaussian error distribution. 4^{th} order of DA computation and 1000 samples were used for each input error FWHM value.

Fig. 4.8 shows that the relative error of the resulting field is strongly reduced in comparison to the input error: the output FWHM of $\Delta B/B(0, 0, -1)$ is in average 789 times smaller than the input FWHM. The error of the derivatives

is larger, but their contribution to the magnetic field is much smaller. Indeed, the mean error of B''_{XZ} of 0.13 (this corresponds to the input error FWHM of 0.01) leads to a maximal relative error of the B_Y estimation of $2 \cdot 10^{-4}$ in the point $(0.2, 0, -0.9)$. The robustness of SIHM against input noise makes it an attractive method to increase the accuracy of the magnetic field measurement data. To apply this method, a Hall probe measurement of all 3 components of $\vec{B}$ needs to be performed on the surface of a cuboid.

4.2 Extension of the method to flat volumes

Although the vertical aperture of Super-FRS dipoles is relative large (±9 cm [53]), the horizontal spread of the beam is about two times larger (±19 cm [53]). Thus, the polynomial expansions resulting from the SIHM are not applicable to describe the field behaviour in the whole transversal cut of the volume of interest. Two different approaches to overcome this problem were tested.

The first approach can be described using Fig. 4.9. The kernel $|\vec{r} - \vec{r}_s|^{-1} =: r_0^{-1}$ of Eqs. (2.21) and (2.22) is analytic in a sphere with radius r_0 around the expansion point P_1 where the DA vector of the magnetic field is sought. The closest singularity P_0 is located on the nearest surface element at a distance r_0 to P_1. However, r_0 is smaller than the half of the horizontal beam spread $a_h/2$. In order to increase the convergence radius the expansion point can be moved by a distance Δr_0 away from P_0 to P_2. For a sufficiently large convergence radius $r_0' = r_0 + \Delta r_0$ the condition

$$r_0'^2 > \Delta r_0^2 + a_h^2/4$$

has to be fulfilled for Δr_0. The expansion polynomial calculated in P_2 can be transformed as if it were expanded in point P_1.

Although this method works in principle, it converges slowly with increasing calculation order. For example, using a 36^{th} order of calculation results in relative errors with an order of magnitude of 10^{-3}. Applying even higher orders might lead to a sufficiently accurate solution but would increase the computational costs to an unacceptable level.

For the second approach the SIHM is used for the computation of low-order DA vectors in a 2D array of points in the volume of interest. Next, subarrays of the DA vectors are fitted by means of higher order polynomials. If a field with midplane symmetry is considered, it is possible to obtain the 3D distribution

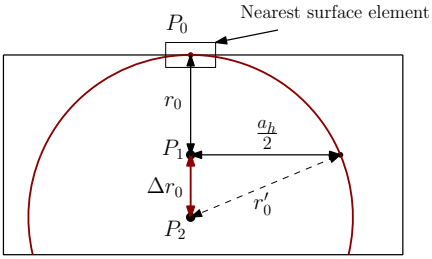

Figure 4.9: Illustration of the first method to resolve the problem with a too small radius of convergence. The rectangular frame corresponds to the transversal cross-section of the cuboid.

of $\vec{B}$ from the 2D distribution of B_Y in the plane $Y = 0$ using the DA fixed point theorem.[1] Therefore, it is sufficient to search for polynomials of the form

$$\sum_{i=0}^{n} \sum_{j=0}^{n-i} c_{i,j} (X - X_{\text{exp}})^i (Z - Z_{\text{exp}})^j \tag{4.2}$$

in the plane $Y = 0$, where $(X_{\text{exp}}, Z_{\text{exp}})$ are the expansion points placed on the reference path.

This approach consists of three steps:

1. A set of locations covering the region of interest was defined as shown in Fig. 4.10 for a reduced number of locations. In the longitudinal (s) direction 299 points were used. The density of these points was chosen higher at the fringes where the field changes rapidly. In the transversal (x) direction 41 evenly spaced points were used.
2. Second order DA vectors were obtained in these locations via the SIHM.
3. A least squares polynomial fit was used to find high-order Taylor polynomials like in Eq. 4.2 with expansion points on the reference path. These points coincided with the corresponding subset of expansion points used in the SIHM procedure. For the fit in every expansion point, subarrays of size 41 in x direction and $M_s > 10$ in s direction were used, where M_s was varied to provide the best accuracy. As input of the fit not only B_Y values, but also their first order derivatives were used, which made the

[1] The method [58] is available in the beam physics package in COSY.

fit numerically stable even for high-order polynomials and equidistantly spaced points. For a polynomial of order n a number $N_c = (n+2)!/(n!2!)$ of coefficients was needed.

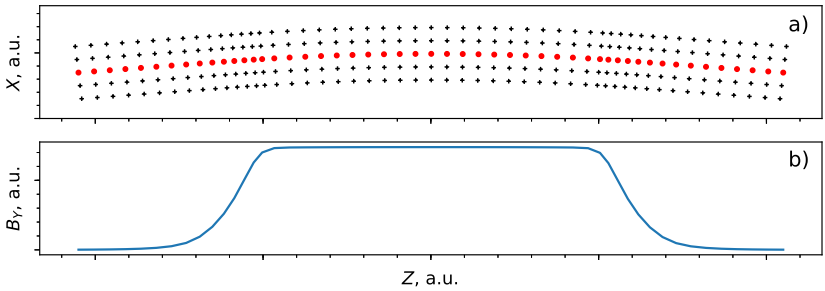

Figure 4.10: A schematic example of a 2D set of expansion points in the plane $Y = 0$ **a)** and corresponding distribution of B_Y **b)**. The red dots in **a)** are located on the reference trajectory.

It should be noted here that the discussed least squares fit with values and derivatives could be used even without SIHM. However, in this case there is no suppression of measurement errors and a smoothing of the initial field data is required to obtain accurate derivatives.

4.3 Polynomial field representation for the Super-FRS preseparator dipole

Before proceeding with obtaining DA-vectors $B_Y(X, Y = 0, Z, I)$, representing the B-field with a good accuracy, it is crucial to set the required accuracy limit. In the considered case the accuracy is limited due to the voltage ripples of the power supplies of the dipole magnets. These ripples have an amplitude of $5 \cdot 10^{-5}$ to 10^{-4} in relative units [7] and produce similarly large ripples in the main field B_0. The FEM solver accuracy was set to $1 \cdot 10^{-6}$ to provide data which could be used for the validation of the obtained DA vectors.

4.3.1 Description of the method

To calculate the DA representation of the magnetic field, a further extension of the SIHM was implemented to add the functional current dependency into the B-field representation. For this the coefficients of the expansion $b^{\alpha}_{0,1,2,\ldots,n}$ of $\vec{B}$ in I (Eq. (4.3)) instead of the field values were used as input for the SIHM procedure in COSY.

$$B_{\alpha}(I) \approx b^{\alpha}_0 + b^{\alpha}_1(I-I_0) + b^{\alpha}_2(I-I_0)^2 + \ldots + b^{\alpha}_n(I-I_0)^n \tag{4.3}$$

Here I_0 is an expansion point in I and $\alpha \in \{X, Y, Z\}$. The coefficients $b^{\alpha}_{0,1,2,\ldots,n}$ were obtained as smooth functions of the coordinates using the SIHM and the vectors $\vec{B}(X, Y, Z, I)$ are obtained by combining the DA values of coefficients using

$$B_{\alpha}(I) \approx b^{\alpha}_0 + b^{\alpha}_1 dI + b^{\alpha}_2 dI^2 + \ldots + b^{\alpha}_n dI^n, \tag{4.4}$$

where dI is a differential unit of I. For the current range of the Super-FRS dipole, the whole $B_{\alpha}(I)$ curve could not be approximated with low order polynomials up to a sufficient accuracy while using higher orders would have required unacceptably large computation resources. Therefore, each $B_{\alpha}(I)$ curve was split into four pieces. A piecewise 4^{th}-order polynomial approximation was performed preserving C^2-smoothness (see Sec. 2.6.2) to obtain functional dependency on each piece. The raw input data used in the extended SIHM is the magnetic field $\vec{B}$ on the surface of the cuboid $\mathscr{D} = \{X \in [-0.6, 0.6]\,\text{m}, Y \in [-0.08, 0.08]\,\text{m}, Z \in [-2.2, 2.2]\,\text{m}\}$ sampled equidistantly with step widths of 4 mm in space and 25 A in current.

4.3.2 Results and discussion

The resulting field, evaluated from 10^{th} order polynomials in the area of interest along the reference path, is in good agreement with the initial simulated magnetic field as is shown in Fig. 4.11.

The area of relatively high errors (up to $\pm 9 \cdot 10^{-5}$) at $s \approx 1\,\text{m}$ and $s \approx 3.2\,\text{m}$ corresponds to the fringe field regions, where the shape of the field is too inhomogeneous to be mapped more accurately by 10^{th} order polynomials. This inhomogeneity originates from the pole end geometry, shown in Fig. 3.4.

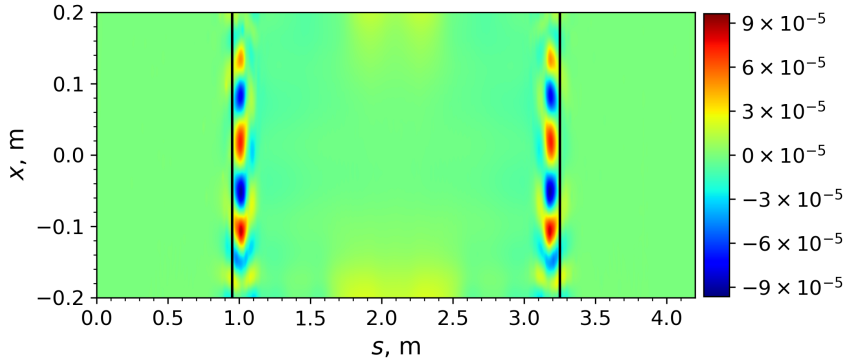

Figure 4.11: Relative difference $\Delta B/B(0,0,0)$ between the initial magnetic field obtained by FEM simulation and the resulting 10^{th} order polynomial approximations evaluated in the midplane along the reference path in curvilinear coordinates for a coil current of 575 A. The black lines indicate the physical borders of the dipole.

The reconstructed off-plane magnetic field reveals higher errors up to one percent in the fringe field region as shown in Fig. 4.12, which is in good agreement with error analysis in [58].

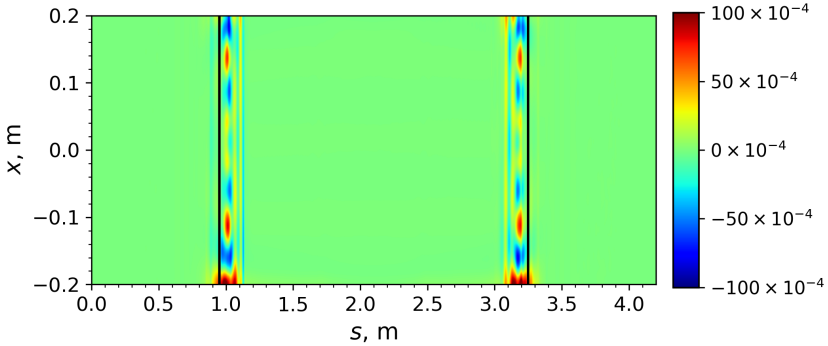

Figure 4.12: Relative difference $\Delta B/B(0, 70, 0)$ between the initial magnetic field obtained by FEM simulation and the resulting 10^{th} order polynomial approximations evaluated in the plane $Y = 70$ along the reference path in curvilinear coordinates for a coil current of 575 A. The black lines indicate the physical borders of the pole shoes.

In Fig. 4.13 the relative integral error is depicted for the approximation of the magnetic field in the aperture of the magnet with polynomials of different orders. The error is oscillating along the x-axis and its amplitude decreases with increasing order. This is a consequence of the mentioned complexity of the form of the fringe field. The mean error has a non-zero value due to the error in the B-I polynomial approximation as well as an error arising from the FEM-simulation. In the figure the results are only shown for 575 A, but they are similar for full current range of the dipole.

Changing the polynomial order a balance between the computation time and the accuracy can be achieved for the considered applications. The quantification of the required accuracy and the computational order for the Super-FRS application requires an insight into the ion optics. This is discussed in Sec. 6.1.

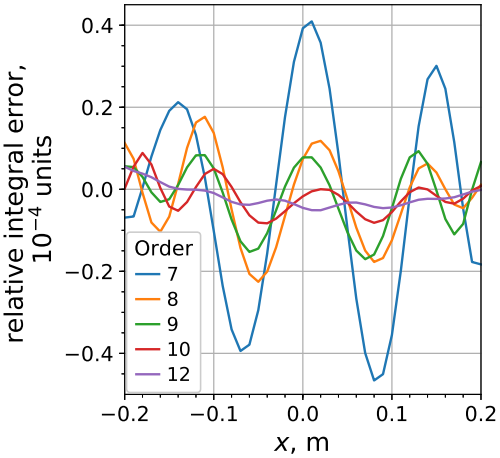

Figure 4.13: Relative integral error $\int (B_Y(x,s) - B_{Y0}(x,s))\,ds / \int B_{Y0}(x,s)ds \cdot 10^4$ with the initial magnetic field from a FEM simulation B_{Y0} and the magnetic field from polynomial approximations B_Y calculated for different orders against the transverse curvilinear coordinate x for a coil current of 575 A. The integration is performed along the path length s.

5 Computation of Taylor transfer maps from 3D magnetic fields

The subject of this chapter is the generation of ion-optical transfer maps starting from measured or simulated magnetic field data. Two different ways to obtain transfer maps utilizing magnetic field information are discussed. The first way is a general method based on the numerical integration of ODEs of motion in the DA framework while the second exploits Enge functions to represent the fringe fields and multipole descriptions of the transversal field non-uniformity. Subsequently, the choice of the reference trajectory choice in a symmetric dipole and the computation of the according rigidity-dependent transfer maps of iron-dominated magnets are discussed. Finally, the general approach for the generation of the transfer maps is verified using the analytical model introduced in Sec. 4.1. The text and images in this chapter are partially adapted from the author's publication [51].

5.1 Transfer map computations using integration of ODEs of motion in the DA framework

To obtain a transfer map in the DA framework it suffices to integrate the ordinary differential equations (ODEs) of motion along the reference path using the DA arithmetic rules. In this work, a 7(8) order Runge-Kutta DA integrator [59, 60] with step size control was used. The resulting transfer map is a solution of the initial value problem

$$\vec{z}_\mathrm{f} = f(s, \vec{z}_\mathrm{i}),$$

where $f(s, \vec{z}_\mathrm{i})$ is described by the Eqs. (2.12) - (2.17) and $\vec{z}_\mathrm{i}$ is the state vector for the initial plane s_i. Hence, the transfer map is an array of DA vectors

$$\vec{z}(s_\mathrm{f}) = (x, a, y, b, l, \delta)^\mathrm{T}, \tag{5.1}$$

which relates the coordinates between the initial and the final plane. Each DA vector of the transfer map is a Taylor polynomial depending on the initial coordinates, which can be evaluated easily. The zero order term of each DA vector is zero, since the transfer map is origin preserving. The higher order terms describe the relative change of the beam physics coordinates. Since the magnetic field is described by DA vectors representing expansions in spatial coordinates, its dependency on the coordinates is translated into the $\vec{z}$ at each integration step. The transfer maps obtained using this method will be denoted as "3D maps" further in this work.

5.2 Transfer map computations using Enge fringe fields

Transfer maps can also be calculated using the long multipole approximation for integral transversal non-uniformities together with the Enge function approximation for the fringe fields. In COSY such maps can be generated using the procedure MS [40], which describes the combined function sector magnet. Within this method, the transfer map of a dipole is a composition of fringe field maps and the main field map. The fringe field maps are compositions themselves and consist of the maps generated by the integration of the ODEs of motion as well as the maps of the negative drifts up to the effective boundary of a magnet [10, 11]. For the main field transfer map, the analytical hard-edge approximation is used [10].

The Enge function with six fitting coefficients $a_1, \ldots, a_6$ is given by following formula,

$$F_{\text{Enge}}(z) = \frac{1}{1 + \exp(a_1 + a_2 \cdot (z/D) + \ldots + a_6 \cdot (z/D)^5)}, \tag{5.2}$$

where $\vec{z}$ is the distance perpendicular to the equivalent hard-edge field boundary and D is the height of the aperture of the magnet. In the MS procedure the input multipole coefficients $n_1, \ldots, n_N$ describe the transverse horizontal non-uniformity of an ideal hard-edge sector dipole field [40]

$$B_Y(x) = B_{y0} \cdot \left[1 - \sum_{i=1}^{10} n_i \cdot \left(\frac{x}{R_0} \right)^i \right], \tag{5.3}$$

where B_{y0} is the main dipole field, R_0 is the dipole deflecting radius, and x is the transversal radial direction. To obtain n_i from the magnetic field distribu-

tion, B_Y has to be integrated along the longitudinal coordinate s for a set of x values in the horizontal beam spread. The integrated B_Y is normalized to the corresponding length of the sector field $\theta_0 \cdot (R_0 + x)$ with a subsequent least squares fit of the resulting integral non-uniformities by Eq. (5.3). The maps obtained by this method will be further called "MS+Enge FF" maps.

A better approximation of the fringe field fall-offs could be achieved by a piece-wise polynomial fit with C^2-smoothness as described in Sec. 2.6. Although the resulting function will not be as easy in use as an elegant Enge function, it will be much more flexible and applicable to any longitudinal field shape. The implementation of the method can be considered as an outlook to this work.

5.3 Setting up the reference trajectory in a symmetric dipole

An essential step for the ion-optical simulation of a particle dynamics in a dipole using measured or simulated field data is to set up the realistic reference trajectory in the magnet coordinates, this means to assign one of the possible realistic trajectories of a particle with central value of $B\rho$ as the reference. This trajectory should be located centrally in the good field area and should be as close as possible to the ideal one. In Fig. 5.1 the chosen reference trajectory for the considered dipole is shown together with the magnetic field distribution along it.

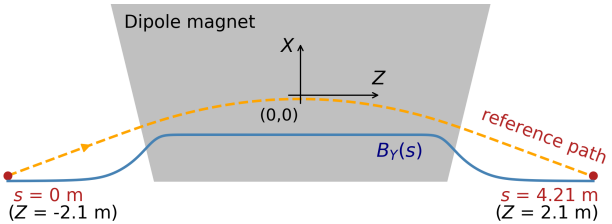

Figure 5.1: Schematic representation of reference trajectory in the magnetic field of the SFRS dipole magnet. The grey trapezoid region corresponds to the projection of the pole shoe geometry onto the midplane.

Traditionally (see, e.g. [11]), the reference trajectory is chosen to fulfill $B\rho = B_0 \cdot R_0$, where $B\rho$ is the particle rigidity and R_0 is the design deflecting

radius. This choice of the reference path is somewhat too idealistic, because it implies that the magnet is built perfectly and its effective length

$$L_{\text{eff}} := \frac{\int_{-\infty}^{\infty} B(S)dS}{B_0} \tag{5.4}$$

(5.4) is equal to the length of the arc in a homogeneous sector magnet.

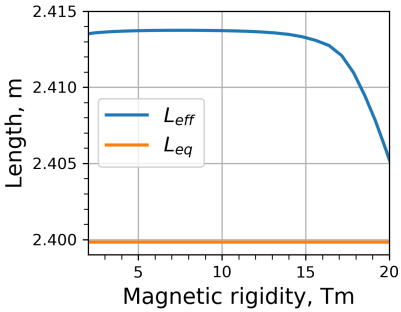

Figure 5.2: The effective L_{eff} and equivalent L_{eq} lengths calculated for the SFRS preseparator dipole versus the magnetic rigidity.

In reality saturation effects always exist. Hence, the effective length is dependent on B_0 and by that also on the rigidity as shown in Fig. 5.2 for the considered magnet. In general, changing the effective length while keeping $B_0 = B\rho/R_0$ forced will lead to various deflecting angles, which might differ from the design value, as shown in Fig. 5.3 **a)**.

The situation can be improved using the equivalent (hard-edge) length

$$L_{\text{eq}} := \frac{\int_{-\infty}^{\infty} B(S)dS}{B_{\text{eff}}} = \int_{-\infty}^{\infty} \frac{B(S)}{B\rho} dS \cdot R_0 = \theta R_0, \tag{5.5}$$

which is equal to the path arclength in a homogeneous sector magnet with a constant field $B_{\text{eff}} = B\rho/R_0$, deflection radius R_0 and deflection angle θ. L_{eq} was introduced as an alternative to L_{eff} in [52][1]. Unlike L_{eff}, L_{eq} is an

[1] In [52] the traditional effective length is named L_{eff0} and the equivalent length is named L_{eff}.

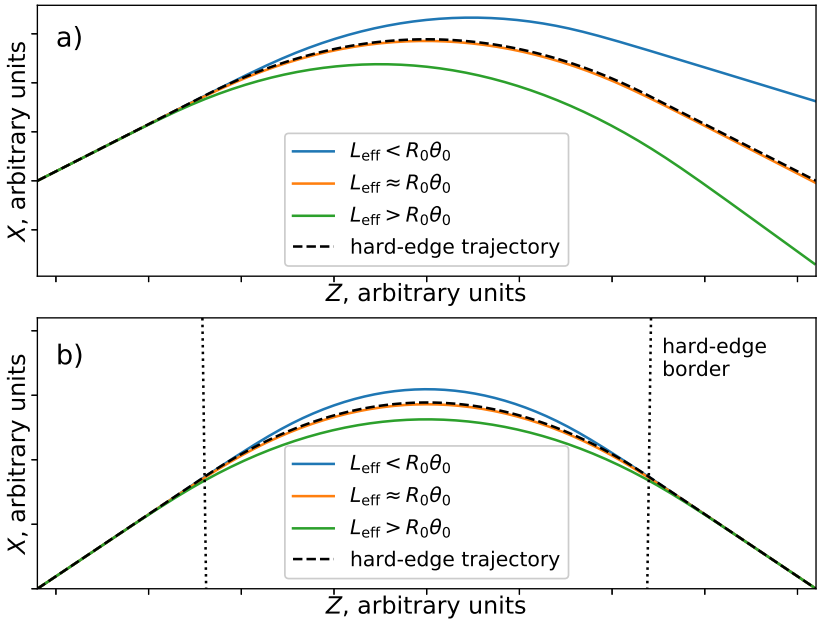

Figure 5.3: Particle trajectories in sector dipoles with different effective lengths L_{eff}. In **a)** the trajectories are set so that $B\rho = B_0R_0$, whereas in **b)** $B\rho = \int_{-\infty}^{\infty} Bds/\theta_0$ is fulfilled.

adjustable parameter, which can be set to a predefined value to achieve the design deflecting angle

$$\theta_0 = \int_S \frac{B_Y(I)}{B\rho} ds \tag{5.6}$$

when varying the coil current. In Fig. 5.2 $L_{\mathrm{eq}}(B\rho)$ is set to a constant value of $R_0\theta_0$. For different relations between the effective and equivalent lengths, this leads to a fixed deflection angle and to slightly different curvatures for the reference particle as depicted in Fig. 5.3 **b)**.

For sector dipoles L_{eq} can also be tuned by varying the position of the reference particle X_{i} at the entrance of the magnet well outside of the field, where $B(X_{\mathrm{i}}, 0, Z_{\mathrm{i}}) \approx 0$. This might be performed by shifting the dipole, which in general can be done only before the first operation of the machine. By tuning both I and X_{i}, one can achieve $L_{\mathrm{eff}} = L_{\mathrm{eq}}$ at utmost two points[2] of $L_{\mathrm{eff}}(B\rho)$ implying the simultaneous fulfillment of Eq. (5.6) and

$$B_0(I) = B(X_0, Y = 0, Z = 0, I) = \frac{B\rho}{R_0}, \tag{5.7}$$

where X_0 corresponds to the position of the reference trajectory in the middle (in Z-direction) of the magnet. In this case the first order transfer map of the magnet will be very close to the transfer matrix of an ideal hard-edge sector dipole with identical values of R_0 and θ_0.

In Tabs. 5.1 and 5.2 the 1$^{\mathrm{st}}$ order transfer maps are presented for the ideal hard edge dipole and for the SFRS preseparator dipole. In both tables, the matrix elements are rounded to 4 meaningful digits. The transfer map of the SFRS preseparator dipole is calculated up to the equivalent field boundary by applying the backwards drifts of the length $(\Delta s - L_{\mathrm{eq}})/2$ to both ends of the map, which is calculated from the beginning of the entrance fringe field to the end of the exit fringe field. Here Δs is the actual arc length of the reference trajectory.

However, the SFRS dipole magnet is effectively longer than it would be in the ideal case, i.e., the effective length for a given B_0 is always greater than the equivalent length. To satisfy both Eqs. (5.6) and (5.7) for the SFRS dipole, a horizontal shifting of the reference trajectory is required. But in this case the beam spread would exceed the good field area which is not acceptable. As a result of the increased effective length, the first order transfer map of the dipole

[2] One for a monotone $L_{\mathrm{eff}}(B\rho)$ and two, if it has a local extremum.

Table 5.1: First order transfer map of an ideal hard-edge sector dipole. The units of the transfer map elements are read as units in the corresponding column heading divided by the units in the corresponding row heading.

	x, m	a, rad	y, m	b, rad	l, m
x, m	0.9816	-0.1526	0	0	-0.1418
a, rad	2.385	0.9816	0	0	-0.1706
y, m	0	0	1	0	0
b, rad	0	0	0.2400	1	0
l, m	0	0	0	0	1
δ, 1	0.1706	0.1418	0	0	0.1504

Table 5.2: First order transfer map of the SFRS preseparator dipole for a particle rigidity of 20 Tm. The units of the transfer map elements are read as units in the corresponding column heading divided by the units in the corresponding row heading.

	x, m	a, rad	y, m	b, rad	l, m
x, m	0.9818	-0.1509	0	0	-0.1417
a, rad	2.385	0.9818	0	0	-0.1706
y, m	0	0	1.001	9.970E-4	0
b, rad	0	0	0.2400	1.001	0
l, m	0	0	0	0	1
δ, 1	0.1706	0.1417	0	0	0.1502

(Tab. 5.1) is slightly different from the ideal hard-edge first order transfer map (Tab. 5.2).

The transfer map elements $(x|x)$, $(a|x)$ and $(a|a)$ are influenced mainly by the form and the length of the fringe field. In contrast, the elements $(l|x)$, $(l|a)$ and $(a|\delta)$ have a dependency only on the deflection as well as on the incident angles and, hence, coincide with the corresponding hard-edge map elements. The difference in the vertical elements $(y|y)$, $(y|b)$, $(b|y)$, $(b|b)$ is a consequence of the inhomogeneity of the magnetic field with non-zero B_X and B_Z values outside of the midplane. The longitudinal dispersion $(l|\delta) = \partial l_\mathrm{f}/\partial\,\delta$ is roughly proportional to the average deflecting radius and is influenced by the fringe field. The transversal dispersion $(x|\delta)$ is dependent on the length of the fringe field as well as on the deflection angle and radius. Moreover, $(x|\delta)$ has nearly equal values for dipoles with slightly different R_0 values but identical equivalent lengths. Most significant for the ion-optical modeling is the difference in the quadrupole element $(a|x)$. Due to the increased L_eff value of the SFRS dipole, $(a|x)$ is smaller than for an ideal sector field.

5.4 Rigidity-dependent transfer maps for iron-dominated magnets

To consider the $B\rho$ dependency in a transfer map, generated using the method described in Sec. 5.1, it is required to introduce the parameter $B\rho$ as a new DA variable in all affected quantities in the equations of motion (2.12) - (2.17). Thus, the rigidity dependency has to be added to the kinetic energy E_k and the magnetic field $\vec{B}$. All other $B\rho$-dependent values can be derived from E_k and $\vec{B}$. $E_k(B\rho)$ can be computed either using a Taylor expansion or a least squares approximation. For wide rigidity ranges the least squares approximation is better: although it has small errors along the entire $E_k(B\rho)$ curve, the whole range $[B\rho_1, B\rho_2]$ can be usually described with a good accuracy by polynomials of relatively low orders. In comparison, the Taylor expansion would lead to fast growing errors with increasing distance from the expansion point due to the strong non-linearity of the $E_k(B\rho)$ function. For the SFRS rigidity range, a least squares fit of $E_k(B\rho)$ with 10^{th} order polynomials yielded a relative accuracy better than $1 \cdot 10^{-8}$.

Adding the $B\rho$ dependency in $\vec{B}$ is a more complex procedure and requires to know the optimal coil current $I_\mathrm{opt}(B\rho)$, for which the reference path coincides with the design trajectory at the entrance and the exit of the magnet, i.e., Eq. (5.6) is satisfied.

To find the function

$$I_{\mathrm{opt}}(B\rho) = C_0^I + C_1^I(B\rho - B\rho_0) + C_2^I(B\rho - B\rho_0)^2 + \cdots + C_N^I(B\rho - B\rho_0)^N, \quad (5.8)$$

an optimization problem

$$\theta = \int_S \frac{B_Y(I_{\mathrm{opt}})}{B\rho} ds \stackrel{!}{=} \theta_0 \quad (5.9)$$

has to be solved. Here $B\rho_0$ is the expansion point preferably placed centrally in the considered $B\rho$ range and $C_0^I, \ldots C_N^I$ are the fit coefficients. The shooting method was used to solve this optimization problem. Due to the linear independence of different order monomials in the DA framework, the fit coefficients can be found individually starting with C_0 and ending with C_N. After obtaining optimal current polynomials, $I(B\rho)$ can be inserted into $\vec{B}(I)$ yielding $\vec{B}(B\rho)$. The resulting $B\rho$-dependent maps can be stored and evaluated for any required particle rigidity for further ion-optical analysis.

5.5 Verification of the transfer maps using the analytical model

The Transfer maps can be verified by means of the Biot-Savart analytical wire model introduced in Sec. 4.1. A transfer map $\mathcal{M}_{\mathrm{if}}$ relates the coordinates $\vec{z}_{\mathrm{i}}$ of the particles in the initial plane to coordinates $\vec{z}_{\mathrm{f}}$ of the particles in the final plane via $\vec{z}_{\mathrm{f}} = \mathcal{M}_{\mathrm{if}} \circ \vec{z}_{\mathrm{i}}$. The initial and final planes are placed perpendicularly to the reference trajectory. Alternatively, $\vec{z}_{\mathrm{f}}$ can be generated by numerical integration of the corresponding equations of motion (tracking).

While tracking of individual particles, it is possible to control the precision using adaptive methods. In this work, an embedded Runge-Kutta method of order 8(7) [61] with automatic stepsize control was utilized. A sufficiently small error tolerance of 10^{-11} was used, which kept the integration time reasonably short.

The transfer map was calculated using truncated analytical as well as SIHM-processed magnetic field DA vectors. In both cases, the DA vectors have truncation errors. The field polynomials obtained with the SIHM contain also error related to the SIHM, which was analyzed in Sec. 4.1. The average errors of the DA representations of the magnetic field were computed with use of $421 \times 21 \times 9$ (in X, Y, and Z directions, respectively) points in the whole volume of interest. The resulting RMS and the maximal relative errors for the

truncated analytic field as well as for the SIHM field are listed in Tab. 5.3 for 12^{th} order.

Table 5.3: RMS and maximum relative errors of the magnetic field data, evaluated from the DA vectors at $421 \times 21 \times 9$ points in volume of interest. The DA vectors were obtained analytically from the wire configuration and by using SIHM. 12^{th} order DA vectors were used in both cases. For comparison the analytical field solution was evaluated in each point.

	RMS error	Max. error
Truncated analytical field	$4.3 \cdot 10^{-11}$	$5.0 \cdot 10^{-10}$
SIHM field	$6.9 \cdot 10^{-9}$	$2.9 \cdot 10^{-7}$

5.5.1 Footprint analysis

An intuitive way to evaluate the accuracy of the transfer map is to compare the *footprints* produced using transfer map and tracking. Here, a footprint is a set of final plane positions of particles produced using a set of regularly spaced positions in the initial plane as illustrated in Fig. 5.4. For the further study, the initial plane was placed at the point $(X, Y, Z) = (-0.1, 0, -2.1)$ in magnet coordinates. The final plane was placed at the point $(X, Y, Z) = (-0.1, 0, 2.1)$. Both planes were normal with respect to the reference trajectory, to provide the same initial and final positions as the transfer map. For convenience the beam physics coordinates are used to describe the positions in the initial $(x_{\text{i}}, y_{\text{i}})$ and in the final planes $(x_{\text{f}}, y_{\text{f}})$.

First of all it is important to estimate the contribution of the truncation errors to the footprint errors. Therefore, the integrated error of the truncated analytical DA field representation was computed for a set of paths parallel to reference trajectory starting in the initial plane and ending in the final plane. The resulting error is shown in Fig. 5.5 for DA vectors of 12^{th} order.

In an area of about ± 6 cm$\times\pm 4$ cm the error is about as high as $6 \cdot 10^{-16}$, which corresponds to a multiple of the machine precision. Towards the outer borders of the plot, the truncation error is growing up to $4 \cdot 10^{-10}$. An analogous error for the magnetic field obtained using SIHM in shown in Fig. 5.6 for 12^{th} order DA vectors, revealing a maximal error of $7.6 \cdot 10^{-9}$. These error values restrict the accuracy of the transfer map generated using the DA field representation.

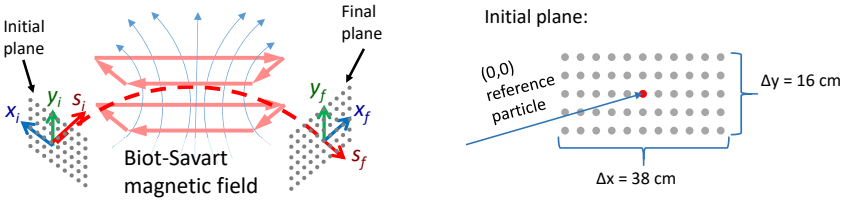

Figure 5.4: Schematic illustration of the footprint analysis. The left hand side shows the mapping of the initial to the final footprints by the Biot-Savart magnetic field. On the right hand side, the positions and dimensions in the initial plane are depicted.

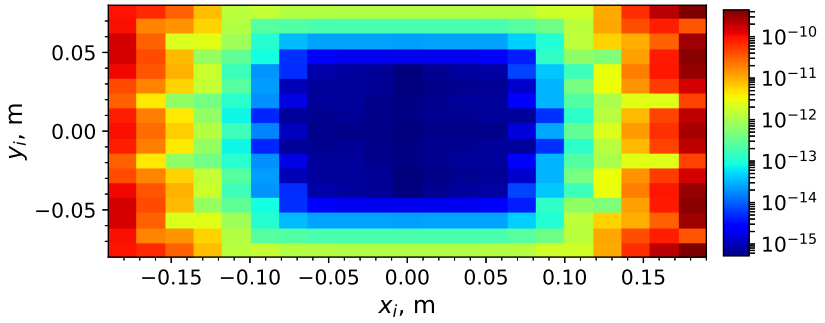

Figure 5.5: Integrated relative error in the 12$^{\text{th}}$ order DA vectors obtained analytically. The integration paths were parallel to the reference path with beginning and ending in the initial and final planes, respectively.

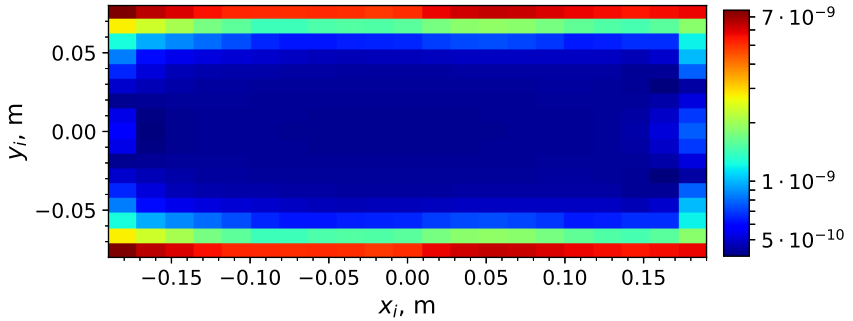

Figure 5.6: Integrated relative error in the 12^{th} order DA vectors obtained with SIHM. The integration paths were parallel to the reference path with beginning and ending in the initial and final planes, respectively.

In Fig. 5.7 the relative difference

$$\Delta_{\mathscr{M},\text{tr}} = \frac{\sqrt{(x_{\text{f, tracking}} - x_{\text{f, }\mathscr{M}})^2 + (y_{\text{f, tracking}} - y_{\text{f, }\mathscr{M}})^2}}{\max(\sqrt{(x_{\text{f, tracking}} - x_{\text{i}})^2 + (y_{\text{f, tracking}} - y_{\text{i}})^2})}$$

in the footprints for tracking and transfer map evaluation is shown. Here, the denominator corresponds to the absolute maximal shift of the considered x, y coordinates due the field distribution between the initial and final planes. In general $\Delta_{\mathscr{M},\text{tr}}$ is larger than the error in the magnetic field representation in Fig. 5.5. For $|x_\text{i}| < 8$ in Fig. 5.7 $\Delta_{\mathscr{M},\text{tr}}$ is as small as $6.5 \cdot 10^{-12}$. This difference is originating mainly from the accuracy restriction in the Runge-Kutta integration. In contrast, for $|x_\text{i}| > 8$ the difference is 3 orders of magnitude higher than in the middle. This growth of $\Delta_{\mathscr{M},\text{tr}}$ is originating from the truncation of the Taylor polynomials of the transfer map.

Indeed, increasing the computation order up to the 14^{th} leads to a reduction of $\Delta_{\mathscr{M},\text{tr}}$ at the borders as shown in Fig. 5.8. Here the maximal difference is $9 \cdot 10^{-10}$ which is about twice as large as the integrated error of the magnetic field truncation.

To conclude, the error in the footprints, which is introduced by the transfer map, is very small. The precision of the transfer map is limited mainly by the accuracy of the polynomial representation of the magnetic field. Since the

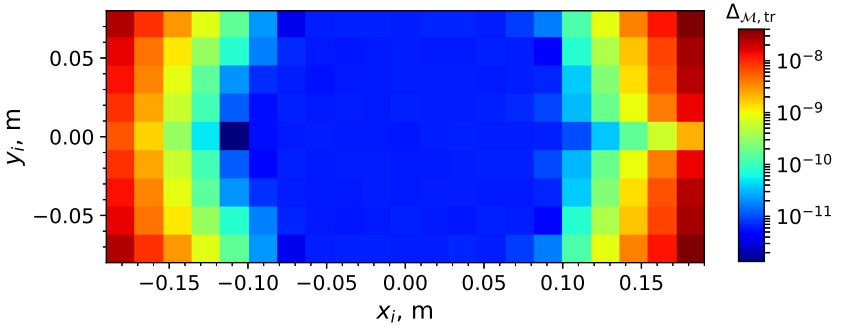

Figure 5.7: Relative difference between the footprints generated using transfer map evaluation and tracking. The transfer map was produced using 12^{th} order DA vectors of the analytical magnetic field.

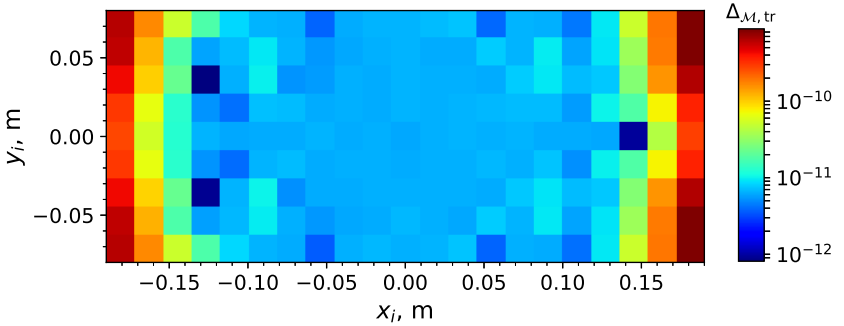

Figure 5.8: The relative difference between the footprints generated using transfer map evaluation and tracking. A 14^{th} order transfer map was generated using the DA vectors of the magnetic field obtained analytically.

magnitude of the error is sufficiently small for the applications in this work, no detailed analysis of the origin of the numerical error or attempts to further reduce it were performed.

5.5.2 Phase space analysis

A more comprehensive way to evaluate the accuracy of transfer maps is to compare the phase space images generated using transfer map and tracking. For this comparison the initial beam physics coordinates were randomly uniformly distributed in the phase volume

$$
\begin{aligned}
&x_\mathrm{i} \in [-0.183\ \mathrm{m}, 0.183\ \mathrm{m}], \quad a_\mathrm{i} \in [-0.219\ \mathrm{mrad},\ 0.219\ \mathrm{mrad}],\\
&y_\mathrm{i} \in [-0.078\ \mathrm{m},\ 0.078\ \mathrm{m}], \quad b_\mathrm{i} \in [-0.513\ \mathrm{mrad},\ 0.513\ \mathrm{mrad}],\\
&\delta_\mathrm{i} \in [-2.5\%,\ 2.5\%],
\end{aligned}
$$

This volume corresponds to a maximal possible illumination of the dipole and a SFRS acceptance.

The transversal projections of the phase space distributions in the initial and final planes are shown in Fig. 5.9. The same planes as in the footprint analysis (Sec. 5.5.1) were used. The TOF coordinate l was equal to zero in the initial plane. For the difference estimation the particles which exceeded the horizontal acceptance $A_h = \pm 0.19\,\mathrm{m}$ or vertical acceptance $A_v = \pm 0.08\,\mathrm{m}$ were excluded from further considerations. The relative difference $\Delta_{\mathcal{M},\mathrm{tr}}$ was computed with respect to the maximal final value for each beam physics coordinate. E.g. for x, the relative difference is

$$\Delta_{\mathcal{M},\mathrm{tr}}(x) = \frac{x_{f,\mathrm{tracking}} - x_{f,\mathcal{M}}}{|A_h|}.$$

The rms and maximal $\Delta_{\mathcal{M},\mathrm{tr}}$ values are shown for each coordinate in Fig. 5.10.

The resulting phase space distributions from transfer maps and tracking are in a very good agreement, even if the field is processed using SIHM, which reduces the precision of the x, a, and I values by about one order of magnitude. For y and b the accuracy might be limited by the computation of the off-plane magnetic field. The maximal error in the a-coordinate has the same order of magnitude as the average field error for the SIHM magnetic field (Tab. 5.3. This can be expected, since $a = p_x/p_0$ is roughly proportional to the integrated B_Y-field. For the directly obtained DA field vectors, a difference in transfer map

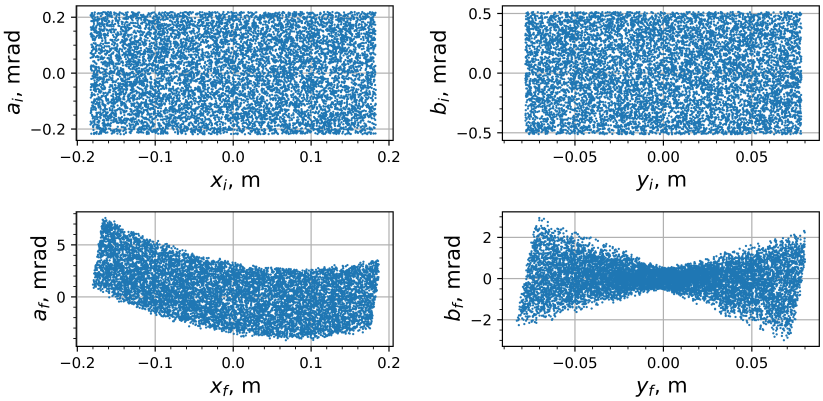

Figure 5.9: Transversal phase space distributions in initial (top) and final (bottom) planes.

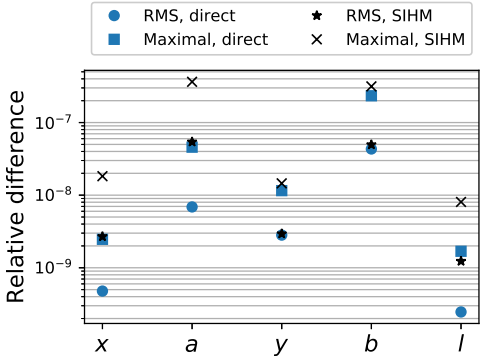

Figure 5.10: Relative differences in 12^{th} order transfer map prediction of the phase space positions in the final plane. The different colors correspond to transfer maps generated from a truncated analytical field (direct) and a field processed using SIHM.

production and tracking algorithms seems to be a dominant contributor to the differences in Fig. 5.10.

Still, the maximal relative difference of about $3.5 \cdot 10^{-7}$ for the a coordinate, is at least two orders of magnitude below the magnitude of current ripples in the dipole power supplies [53] and, hence, does not play an important role in the SFRS ion-optical computation.

6 Application: Super-FRS preseparator optics

In this chapter an ion-optical study of the Super-FRS preseparator including a realistic transfer map of the dipole is conducted. The choice of the computational order and the fitting of the preseparator optics are discussed. The impact of the saturation in the dipoles on the separation was analyzed in both separator and spectrometer modes. The effect of the errors in the dipole excitation currents on the beam dynamics was estimated. Finally, the 3D and MS+Enge FF maps were compared. 3D maps were used everywhere in this chapter except in the Sec. 6.7. The text and pictures in this chapter are partially adapted from the author's publication [51].

6.1 Ion-optical layout of Super-FRS preseparator

The Super-FRS preseparator schematically depicted in Fig. 6.1 is a $B\rho$-ΔE-$B\rho$ separator with two deflecting stages and a wedge energy degrader between them. Each deflecting stage has a triplet of similar 11° dipoles. There are four focal planes in the Super-FRS preseparator. The most interesting planes are the dispersive focal plane FPF2, where the degrader is placed, and the achromatic focal plane FPF4 at the end of the preseparator. A detailed description of the ion-optical layout of the preseparator can be found in [62]. For focusing and correction of geometric and chromatic aberrations quadrupoles, sextupoles and octupoles are used.

To study the impact of the $B\rho$ dependency and high order aberrations on the resolution of the Super-FRS preseparator, the $B\rho$ dependent maps of the dipoles were inserted into the ion-optical model in COSY INFINITY. For the multipole elements the standard COSY Enge fringe fields were used. There are two modes of operation of the Super-FRS preseparator: separator mode and spectrometer mode. In the separator mode the allover layout of the preseparator is achromatic for the nuclei to be selected (see rays in the Fig. 6.1). The wedge degrader, placed in the dispersive FPF2, reduces the energy of the nuclei depending on their charge state and hence grants the spatial separation

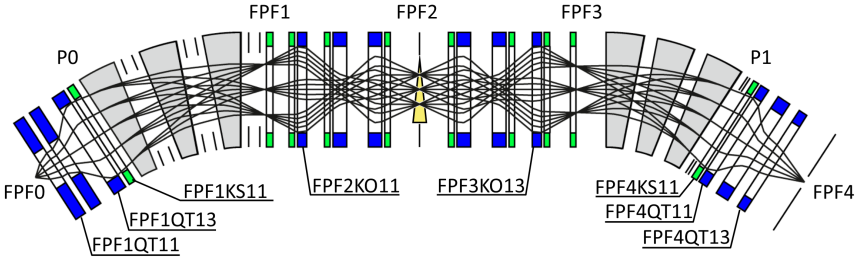

Figure 6.1: Ion-optical layout of the Super-FRS preseparator with production target at FPF0 and focal planes FPF1-4. In the plane FPF2 the wedge energy degrader can be placed. The gray sectors denote dipole magnets, blue-marked elements quadrupoles (sometimes with octupole correctors) and light green-marked elements sextupoles. The rays produced for 5 initial angles and 3 initial energies demonstrate the achromatic layout of the Super-FRS preseparator. More labels are used for further discussion.

of the nuclei with different atomic numbers at the FPF4. In the spectrometer mode the dispersions of the stages are added up. This allows to produce high-resolution $B\rho$ spectra of isotopes.

6.2 Choosing the order of the ion-optical model

Before proceeding with ion optical studies it is important to find out which order of approximation is sufficient for calculating the transfer maps of the dipole for the Super-FRS application. A comparison of the horizontal phase space images at FPF4 for different orders and the same initial coordinates is shown in Fig. 6.2. For the sake of simplicity the subject of comparison are the image aberrations of particles with initial distributions lying on concentric ellipses in the horizontal phase space. To generate these images, the same multipole strengths for quadrupoles, sextupoles and octupoles were used. It is clearly seen that for an emittance $\leq$22.5 mm·mrad, the resulting image does not change significantly beyond the 7^{th} order. For an emittance of 38 mm·mrad, corresponding to the maximal acceptance of the Super-FRS, the image stabilizes only after the 12^{th} order, since the lower orders display incorrect behavior of the top and bottom ends of the final phase space.

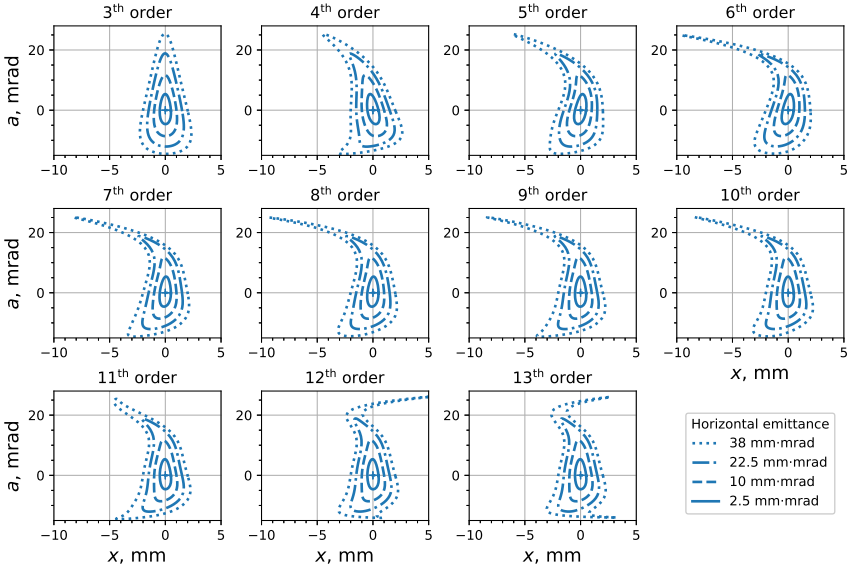

Figure 6.2: Horizontal phase space images at FPF4 for different order transfer maps. The initial coordinates are given by functions $(x_k \cdot \cos(\phi), a_k \cdot \sin(\phi), 0, 0, 0)$ with $\phi \in [0, 2\pi)$, $x_k \in [0.25\,\text{mm},\ 0.5\,\text{mm},\ 0.75\,\text{mm},\ 1\,\text{mm}]$ and $a_k \in [10\,\text{mrad}, 20\,\text{mrad}, 30\,\text{mrad}, 38\,\text{mrad}]$.

Various inclinations of the phase space for low orders originate from the least squares fit approach to the magnetic field representation: the least squares polynomials of different degree do not have the same low order terms.

6.3 Fitting the preseparators optics

For the best separation, the beam spot at FPF4 has to be minimized, which can be performed by reducing the first and second order geometric (primarily horizontal) and chromatic aberrations in the focal planes via fitting of the multipole strengths. All multipoles of the preseparator (12 quadrupoles, 10 sextupoles and 4 octupoles) can be tuned to achieve optimal settings for the $B\rho$ range from 2 to 20 Tm and maintain the first order ion-optical layout described in [62].

Besides reducing the aberrations and maintaining the first order layout of the separator, some transfer map elements were deliberately fitted with an offset to improve the overall transmission. The offsets used in this work were determined by the GSI Super-FRS group. The element $(a|\delta\delta)$ at FPF2 was fitted to $(0.0003/\delta^2_{max})$ in order to reduce the maximal current of the sextupole FPF2KS11 (see Fig. 6.1) for a rigidity of 20 Tm. Although the last offset is only required for 20 Tm, it was kept for all rigidities in order to provide always the same fit conditions. All objective transfer map elements, their desired values and the transversal planes of their acquisition are listed in Tab. 6.1. The horizontal beam width inside the dipoles had to be kept constant by controlling the corresponding transfer map elements in the planes before the first dipole P0 and after the last dipole P1. This was required for preserving the first order resolving power at FPF2

$$R_{1,FPF2} = (x|\delta)/((x|x)\Delta x_i) \approx -2.6/(1.65\Delta x_i), \tag{6.1}$$

which corresponds to $p/\Delta p = 1576$ for $\Delta x_i = 1$ mm.

Optimal multipole settings were obtained with the help of the multiparametric fit-procedure in COSY via the Levenberg-Marquardt algorithm [63]. Since the maximal order of the multipole elements is three, the fitting was performed using transfer maps truncated up to 3$^{\text{rd}}$ order.

There is an alternative to truncating the transfer maps to 3$^{\text{rd}}$ order for the fitting. It is generating 3$^{\text{rd}}$ order maps from 3$^{\text{rd}}$ order polynomial representation of the magnetic field, based on a least squares fit (further such maps will be named LS maps). In Fig. 6.3 the integral non-uniformity of the Super-FRS

Table 6.1: Transfer map elements used as objectives for the optimization of the settings of the Super-FRS preseparator. The elements without description are optimized for reducing aberrations. The units of a transfer map element $(z_{jf}|z_{ki})$ correspond to a fraction with the units of z_{jf} in the numerator and the units of z_{ki} in the denominator. If several quantities are placed after the "|" symbol, the denominator is equal to the product of all corresponding units. (x, a, y, b, l, δ) have the units of (m, rad, m, rad, m, 1).

Plane	Element	Desired value	Description
P0	$(x\|a)$	0.172	Value to preserve 1st order resolution
P0	$(b\|b)$	0	Lattice parameter.
FPF1	$(x\|a)$	0	
FPF2	$(x\|a)$	0	
FPF2	$(y\|b)$	0.05	An offset for better transmission
FPF2	$(y\|\delta)$	0	
FPF2	$(x\|aa)$	0	
FPF2	$(x\|a\delta)$	0	
FPF2	$(x\|\delta\delta)$	0	
FPF2	$(a\|\delta\delta)$	$0.0003/\delta^2_{max}$	An offset to reduce max. current in FPF2KS11.
FPF2	$(y\|b\delta)$	0	
FPF2	$(x\|\delta\delta\delta)$	0	
FPF3	$(b\|b)$	0.03	An offset for better transmission
P1	$(x\|\delta)$	0	
P1	$(a\|\delta)$	0	
FPF4	$(x\|a)$	0	
FPF4	$(y\|b)$	0.0012	An offset for better transmission
FPF4	$(x\|x)$	2	Value to preserve 1st order resolution
FPF4	$(x\|aa)$	0	
FPF4	$(x\|a\delta)$	0	
FPF4	$(x\|\delta\delta)$	0	
FPF4	$(a\|\delta\delta)$	0	
FPF4	$(y\|b\delta)$	0	
FPF4	$(x\|aaa)$	0	
FPF4	$(x\|\delta\delta\delta)$	$20\frac{\Delta p_{max}}{\delta^2_{max}}$	An offset for better transmission

preseparator dipole together with its 3rd order least squares fit and its 3rd order Taylor expansion around the point $x = 0$ is shown. It is obvious that fitting of the preseparators optics will lead to different optima for the truncated transfer maps and the LS maps.

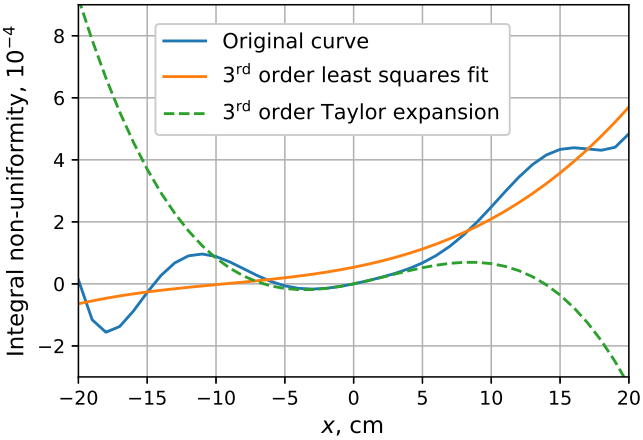

Figure 6.3: The integral non-uniformity of the magnetic field of the NC Super-FRS preseparator dipole for $I = 575$ A together with its 3rd order Taylor expansion and least squares fit.

In Fig. 6.4 the phase space distributions generated with 13th order optics and optima obtained using LS as well as truncated maps are shown. Depending on the particular experimental application either 3rd order transfer maps can be used for the fitting. If it is important to capture a maximal number of particles from the whole phase volume, the best option would be to perform the fitting using LS maps. Although the resulting horizontal phase space is convex for small x and a (Fig. 6.4 **a)**), the fit conditions lead to the best confinement of the whole beam. Controversially, if only a small fraction of the phase space is required, the best option would be to use truncated high order maps for the fitting. Indeed, in Fig. 6.4 **b)** the area with high density in the middle of the spot is slightly more upright and narrow than in Fig. 6.4 **a)**.

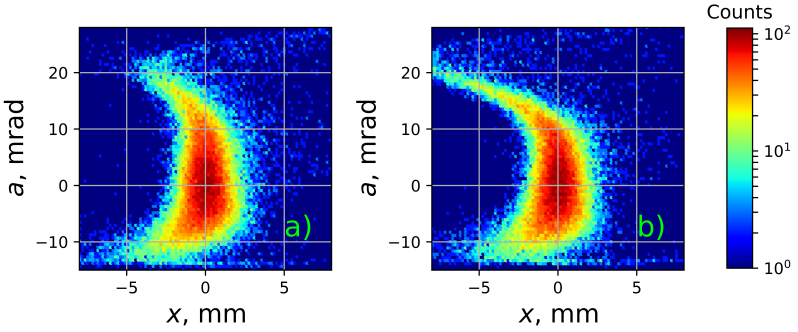

Figure 6.4: The transverse horizontal phase space distribution in the FPF4, generated using 13$^{\text{th}}$ order computation. The optimal multipole strengths were obtained with dipole maps, generated using a 3$^{\text{rd}}$ order least squares B field representation **a)**, and with dipole transfer maps of 3$^{\text{rd}}$ order, obtained via truncation of 13$^{\text{th}}$ order maps **b)**.

Discussion of the optimal multipole settings

The dependencies of the optimal multipole strengths in preseparator optics on $B\rho$ (Fig. 6.5) have very similar shapes compared to the corresponding integral non-uniformities in the dipole magnet field distribution (Fig. 6.6) although with different sign to compensate the effect of the dipoles. The magnets chosen for comparison are labeled as in Fig. 6.1. The curve for octupole FPF3KO13 in Fig. 6.5 has a deviating shape, which is likely influenced by the vertical octupole component of the dipole and by thevertical fit conditions. The vertical octupole component is not shown here but it has a similar characteristic as the horizontal sextupole component in Fig. 6.6 with a different sign.

In Tab. 6.2 and 6.3 the mean integral multipole components of the dipole and the discussed preseparator multipoles normalized with respect to $B\rho$ are presented, respectively. From these numbers it can be deduced that the mean quadrupole component of the dipole is about as large as 4% of the quadrupole strengths of FPF1QT13 and FPF4QT11, the mean sextupole component of the dipole is 16% of FPF1KS11 and the mean octupole component of the dipole is 12% of FPF2KO11. These values roughly explain the correspondence between the relative change spreads in Figs. 6.5 and 6.6.

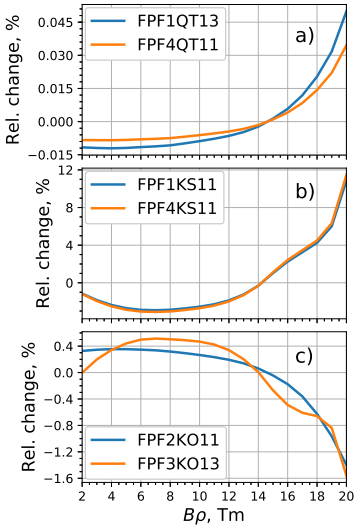

Figure 6.5: Relative change of the optimal multipole strengths versus the particle rigidity $B\rho$ for two quadrupoles **a)**, two sextupoles **b)** and two octupoles **c)** labeled in Fig. 6.1.

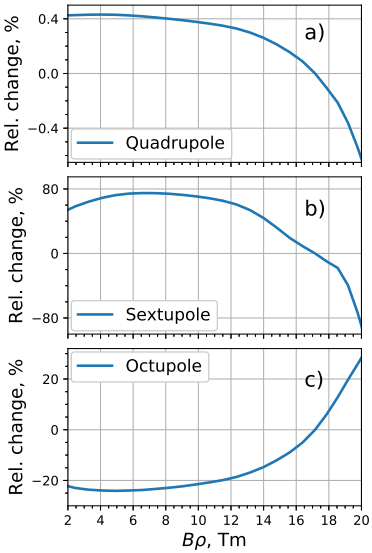

Figure 6.6: Relative change of the dipoles integral horizontal non-uniformities of **a)** 1st (quadrupole), **b)** 2nd (sextupole) and **c)** 3rd (octupole) orders versus the particle rigidity.

Table 6.2: Mean integral multipole components of the Super-FRS dipole normalized with respect to the magnetic rigidity.

Quadrupole	0.015 m^{-1}
Sextupole	-0.003 m^{-2}
Octupole	0.027 m^{-3}

Table 6.3: Mean integral multipole strengths for selected Super-FRS quadrupoles, sextupoles and octupoles normalized with respect to the magnetic rigidity.

FPF1QT13	0.356 m^{-1}
FPF4QT11	0.353 m^{-1}
FPF1KS11	-0.0206 m^{-2}
FPF4KS11	-0.0172 m^{-2}
FPF2KO11	-0.146 m^{-3}
FPF3KO13	-0.0923 m^{-3}

6.4 Separator mode

In order to study possible changes caused by magnetic saturation to the predicted separation, a numerical experiment with tracking of two fragments of ^{238}U from a carbon target was performed. The fragments ^{216}Pa and ^{215}Th with a rigidity of 20 Tm were tracked inside the preseparator including the energy loss in copper wedge degrader, which is designed to slow the reference particle (^{216}Pa) down to 14 Tm. In this case the resolution is limited by the inevitable energy loss straggling in the degrader, which was taken into account using the theory in [64]. The average energy loss was calculated using the Bethe-Bloch formula. For computational convenience, all the tracking was performed using a rigidity of 20 Tm, whereas the energy/momentum deviations and transfer maps were scaled appropriately. Particles with a phase space exceeding the local acceptance were excluded from further tracking.

To observe the maximal change in the separation caused by magnetic saturation, the images on the horizontal phase space were compared. The resulting phase space distribution for 2 and 20 Tm (borders of the Super-FRS $B\rho$ range) can be seen in Fig. 6.7, where dark blue and dark green dots correspond to the system with maps as for 2 Tm and cyan and lime dots correspond to the system with maps for 20 Tm. In both cases the initial beam phase space after the production target was the same: $(x, a, y, b, \delta) = \pm(0.5\,\text{mm}, 38\,\text{mrad}, 2\,\text{mm}, 20\,\text{mrad}, 2.5\%)$. Although the effect of magnetic saturation on the images of the ^{216}Pa and ^{215}Th on the achromatic focal plane FPF4 can be distinguished

in the Fig. 6.7, its magnitude is so small that it has no meaningful effect on the resolution.

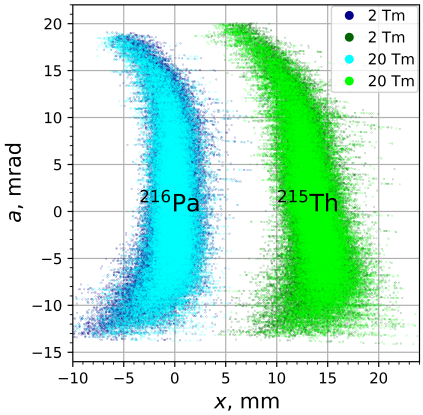

Figure 6.7: Horizontal phase space images of the separation of fully-stripped 20 Tm ^{216}Pa and ^{215}Th after the preseparator including the copper wedge degrader, which slows the reference particle (^{216}Pa) down to 14 Tm. In the preseparator optics the transfer maps of the dipole magnets for 2 Tm (dark dots) and 20 Tm (light dots) were used to detect the maximal effect of the magnetic saturation on the separation.

6.5 Spectrometer mode

Besides the separation mode, the Super-FRS can be used as a high-resolution spectrometer. In this case the dispersion of many stages is added up. Here such a case with four stages was simulated to see the effect of saturation on the resolution. This simulation did not include the ion optics of the entire Super-FRS, but repeated the first stage of the Super-FRS preseparators four times. The optimal multipole settings for 16 Tm were used for all other rigidities too. To distinguish the saturation-caused aberrations, the magnification was artificially compensated at all stages except for the last one.

In Fig. 6.8 **a)** the resulting horizontal phase space is shown for 9 monoenergetic slices, which were evenly distributed within $\Delta p/p = \pm 4.8 \cdot 10^{-3}$ and had identical initial distributions in their geometrical phase volume. The biggest change is happening between 16 Tm (green dots) and 20 Tm (red dots), whereas the difference between the distributions from 2 to 16 Tm is insignificantly small. The histogram in Fig. 6.8 **b)** reveals a slight broadening of the peaks introduced by the non-compensated saturation. If the optimal settings for each rigidity are used, the difference practically vanishes, as shown in Fig 6.8 **c)**.

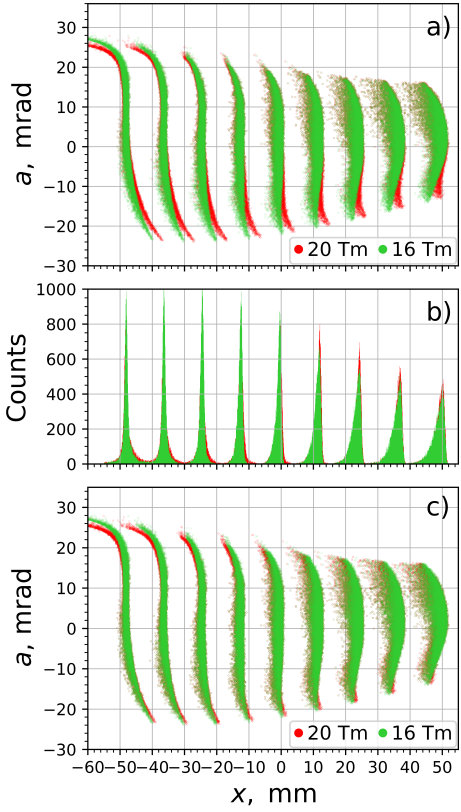

Figure 6.8: Horizontal phase space at the dispersive focal plane after passing through 4 dipole stages in the spectrometer mode for rigidities of 16 Tm and 20 Tm. **a)** the optimal multipole setting for 16 Tm is taken for both cases. **b)** the number of counts along the x-axis for the phase space. **c)** individual optimal multipole settings were used.

6.6 Effects of errors in dipole excitation currents

Setting the correct excitation currents in ion-optical elements is crucial for reliable accelerator operation. Whereas in multipoles the errors in the current cause aberrations of first and higher orders, the errors in dipole currents lead to a shift of the entire beam, which, in the worst case, causes beam loss and consequences thereof like destruction of material due to ionization and heat load or quench in superconducting coils.

To find out the current required for a given rigidity, the excitation curve $B(I)$, integrated along the reference trajectory is used. The values of the integral excitation curve (IEC) normalized to $B\rho$ equal a deflection angle. Hence, the design deflection angle θ_0 can be achieved for a given $B\rho$ by varying the current so that

$$\frac{1}{B\rho}\int_{S_0}^{S_1} B_y(I)(X(S),0,Z(S))dS = \theta_0. \tag{6.2}$$

Practically, the integration is often performed along a line which is parallel to the Z-axis and fulfills

$$\int_{Z_0}^{Z_1} B_y(X_{IC},0,Z)dZ = \int_{S_0}^{S_1} B_y(X(S),0,Z(S))dS. \tag{6.3}$$

Here X_{IC} is an unknown parameter. Using measurements, X_{IC} can be found with help of a Hall probe mapping data by solving a simple root-finding problem. For this, Brent's method [65] in the python package scipy.optimize [66] can be used. The integral field can also be measured directly by means of a moving stretched wire techniques [67] or moving long curved search coils [68].

If an IEC from simulations is used in setting the operation current, the difference between the actual and the simulated magnetic field will lead to various deflection angles and shifts of the beam positions in the dispersive planes. In the case of the NC Super-FRS preseparator dipole, the maximal relative difference between the measured and the simulated IEC of 0.6% leads to an offset of 15 mm at FPF2 as depicted in Fig. 6.9. This indicates that accurate measurements of IES are required for a successful operation of the Super-FRS. A

measurement error of 10^{-4} which is typical for moving stretched wire techniques will lead to an offset of 0.25 mm at FPF2. This offset is relatively small in comparison to the spot size of ±1 mm.

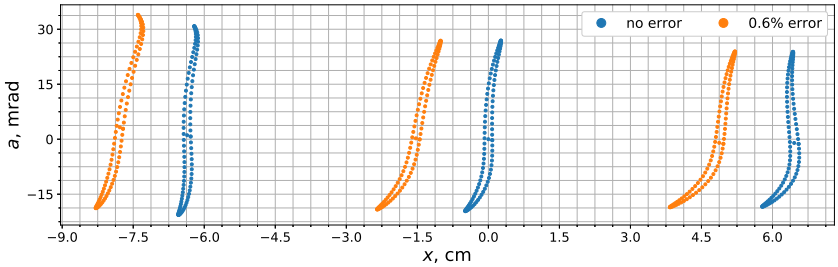

Figure 6.9: Horizontal transverse phase space images at FPF2 without error and with error of 0.6% in dipole coil current. The left, middle and right spot positions correspond to $\Delta p/p$ values of +2.5%, 0 and -2.5%, respectively.

6.7 Comparison of 3D and MS+Enge FF maps

Whereas 3D maps are universal and can be generated for arbitrary magnetic field distributions with midplane symmetry, the MS+Enge FF maps can be obtained relatively quickly and, hence, are more convenient for practical applications. Despite the MS+Enge FF maps do not correspond to any physically possible field distribution, they still might represent the system with a good accuracy.

In Tabs. 6.4 and 6.5 the transfer maps truncated after the second order are shown for a 3D map and for a Enge+MS map, respectively. The first five columns correspond to the end coordinates. The column "Exponents" corresponds to the expansion coefficients in initial coordinates $(x_i, a_i, y_i, b_i, l_i, \delta_i)$, e.g. the Exponent 101000 means $1/(\partial x_i \partial y_i)$. As is seen from the transfer maps all first order coefficients are in good agreement for 3D and Enge+FF maps revealing the relative difference of less than 1% except for the dispersion, $(x|\delta)$, with the relative difference of 2%. This can be due to different longitudinal shapes of the magnetic field fringes. The differences between the both maps in the second order are of up to 10% (for very small elements the difference is larger, but these elements are irrelevant), but their impact on the ion-optical simulation is smaller.

Table 6.4: Second order 3D transfer map.

x	a	y	b	l	Exponents
0.9819	-0.15038	0	0	-0.1471	100000
2.38539	0.981900	0	0	-0.1771	010000
0	0	1.001	9.450E-4	0	001000
0	0	2.39991	1.001	0	000100
0	0	0	0	1	000010
0.1771	0.1471	0	0	0.1166	000001
-1.193E-3	1.198E-4	0	0	-1.902E-4	200000
0.1748	2.913E-4	0	0	3.059E-4	110000
0.1052	-8.867E-02	0	0	-0.9195	020000
0	0	-0.3640E-4	-1.504E-3	0	101000
0	0	-1.787	-1.813E-3	0	011000
-1.693E-3	-1.341E-03	0	0	-5.141E-3	002000
0	0	0.2034	-3.050E-03	0	100100
0	0	0.2448	0.1745	0	010100
-0.1756	-2.022E-03	0	0	-4.822E-4	001100
-0.3348	-0.1057	0	0	-0.9185	000200
2.735E-2	3.692E-4	0	0	9.962E-3	100001
-1.806	1.208E-3	0	0	1.199E-2	010001
0	0	-1.420E-3	1.0478E-2	0	001001
0	0	-1.838	2.480E-2	0	000101
-0.1413	-4.925E-3	0	0	-0.1441	000002

Table 6.5: Second order MS+Enge FF transfer map.

x	a	y	b	l	Exponents
0.9818	-0.1509	0	0	-0.1482	100000
2.38532	0.9818	0	0	-0.1759	010000
0	0	1.002	1.706E-2	0	001000
0	0	0.2400	1.002	0	000100
0	0	0	0	1	000010
0.1808	0.1482	0	0	0.1160	000001
-2.866E-4	1.408E-3	0	0	-9.110E-5	200000
0.1911	0.3330E-2	0	0	-4.673E-4	110000
0.1103	-9.319E-2	0	0	-0.9187	020000
0	0	-3.290E-3	-4.056E-3	0	101000
0	0	-0.1958	-4.847E-3	0	011000
-2.676E-3	2.039E-3	0	0	-5.062E-3	002000
0	0	0.1898	6.103E-3	0	100100
0	0	0.2315	0.1846	0	010100
-0.1963	3.490E-3	0	0	3.922E-4	001100
-0.3481	-9.902E-2	0	0	-0.9182	000200
2.820E-2	1.842E-4	0	0	1.000E-2	100001
-1.804	-2.954E-5	0	0	8.115E-3	010001
0	0	-3.691E-3	1.015E-2	0	001001
0	0	-1.840	2.488E-2	0	000101
-0.1441	-4.990E-3	0	0	0.1436	000002

For a more quantitative comparison, 3D and MS+Enge FF maps were inserted into Super-FRS preseparator ion-optical simulations. A study of the differences in the phase space distribution in the focal planes and the optimal multipole settings was performed. In Fig. 6.10 the horizontal phase space at the dispersive focal plane FPF2 is compared for both approaches for particles with $\Delta p/p = -2.5\%$ (right), 0 (middle) and +2.5% (left) and initial coordinates distributed over 4 concentric ellipses

$$x_i \in \{0.25x_{max}, 0.5x_{max}, 0.75x_{max}, x_{max}\}$$

and

$$a_i \in \{0.25a_{max}, 0.5a_{max}, 0.75a_{max}, a_{max}\}.$$

In both cases the optimal setting for 3D maps on 16 Tm were used. For $\Delta p/p = 0$ a difference in x of about 1 mm is observable for the maximum of a. For $\Delta p/p = \pm 2.5\%$ the main effect is the shifting of the flanks at about 0.5 mm towards outside for MS+Enge FF due to different dispersion. This shift is insignificant in comparison with the beam spots.

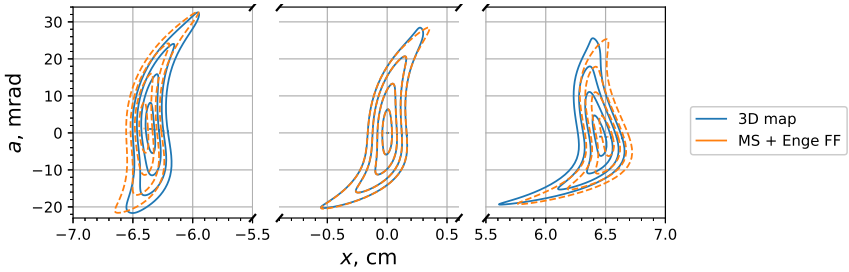

Figure 6.10: Horizontal phase space at FPF2 using 3D map v.s. MS+Enge FF. In both cases the optimal setting for 3D maps with 16 Tm were used. The left, middle and right spot positions correspond to $\Delta p/p$ equal +2.5%, 0 and −2.5%, respectively.

In Fig. 6.11 the normalized relative multipole strength changes are shown for four quadrupoles, two sextupoles and two octupoles. These multipoles are rather representative and demonstrate a very good agreement for the shape of the optimal settings. The deviations in the absolute values are coming from the inequality of the lower order terms for the 3D and the MS+Enge FF maps, which results in different optima. This inequality is partially coming from the

impossibility to obtain a perfect coincidence of the Enge-functions and the real fringe fields. Whereas the Enge functions tend to have steep shoulders, the shoulders of the saturated magnetic field are slightly flatter and it does not have a so called constant field region as is illustrated in Fig. 6.12.

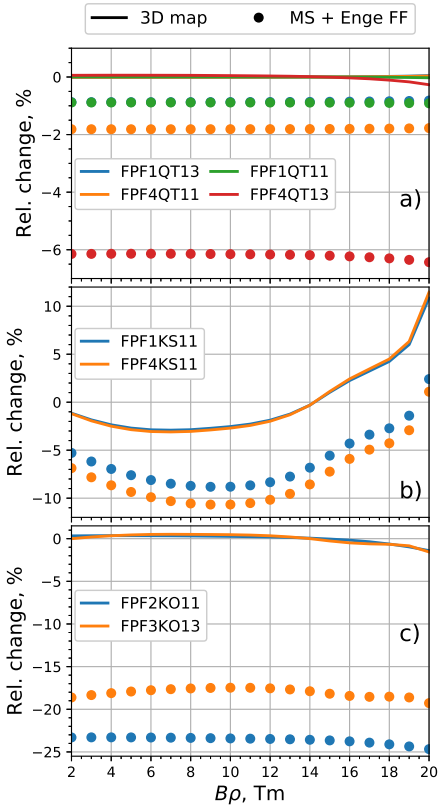

Figure 6.11: Dependence of the relative optimal multipole strengths on the particle rigidity $B\rho$ for the four quadrupoles **a)**, two sextupoles **b)** and two octupoles **c)** comparing 3D maps and MS+Enge FF.

The MS+Enge FF approach appears to be useful to find good operation settings quickly. The deviation in the transverse horizontal phase space distributions between the two methods is very small for the FPF2. Nevertheless, the entire Super-FRS is about 7 times longer and a larger difference for the quadrupoles is expected.

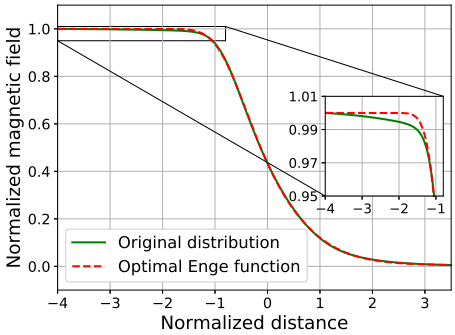

Figure 6.12: Normalized magnetic field against the normalized distance (in units of full vertical aperture) together with its Enge function representation for a magnetic rigidity about 20 Tm. The origin of the abscissa corresponds to the effective field boundary and the negative values correspond to the area inside of the magnet.

7 Summary and outlook

The magnets of charged particle spectrometers and separators play a decisive role for the beam quality and transmission percentage, especially for systems with large geometrical and momentum acceptances. In the case of the Super-FRS, undesired high-order aberrations are expected due to the large usable apertures of the magnets (38 cm × 14 cm for the dipoles and 19 cm × 19 cm for the multipoles) and the wide operation rigidity range (2-20 Tm). Frequent changes of $B\rho$ during the Super-FRS operation are required for tuning and selecting of different nuclides. Moreover, the ion-optical configuration of the Super-FRS can be switched between the separator and the spectrometer modes. Therefore, it is crucial to have a fast and reliable ion-optical model with a good predictability at any rigidity and any combination of the multipole strengths.

Within this work, a general approach has been developed to generate precise high-order Taylor transfer maps, starting from a computed or measured 3D magnetic field distribution. The functional dependence of the magnetic field on the coordinates and the coil current was obtained by combining the SIHM and least squares methods. The harmonic property of the resulting B-field polynomials was maintained. The transfer maps were generated by numerical integration of the equations of motion in the DA framework. The estimated rms relative error in the resulting transfer maps caused by the SIHM method and the numerical integration was smaller than $6{\cdot}10^{-8}$.

The developed approach has been applied to the NC radiation-resistant dipole magnet of the Super-FRS preseparator. For the dipole accurate 3D FEM magnetic field simulations including the measured magnetization curve of the yoke material were conducted. The results of FEM simulations were verified with the measurement data. A study of the method's robustness against noisy data was performed, revealing a strong suppression of the magnetic field errors by the algorithm, which enables the use of measured magnetic field data as input. The universality of the method allows its application not only to the Super-FRS magnets, but also to any other large-aperture magnet.

An ion-optical study of the Super-FRS preseparator with derived rigidity dependent transfer maps was conducted. For the maximal horizontal emittance

of secondary ion beams the 12^{th} order transfer maps of the dipole were required to grant an adequate description of the beam dynamics. The consequences of the shortening of the effective length of the dipoles due to the saturation of the yoke were completely eliminated by introducing the concept of the equivalent hard-edge length. The highest order Super-FRS multipoles are the octupoles (3^{rd} order), which restricts the possibility of the compensation of image aberrations. Special transfer maps were generated using 3^{rd} order least squares approximation of the magnetic field non-uniformities. This allowed the optimization of the multipole strengths for large-emittance beams, which can be helpful to achieve the best capture of rare nuclei with low production rates.

The resulting ion-optical model revealed a slight dependence on the rigidity due to the saturation in the NC dipoles. This effect could be well compensated by optimizing the multipole strengths for individual rigidities. The influence of the error in the simulated optimal coil current on the beam dynamics was studied. The resulting horizontal shift of the beam of 1.5 cm for low currents has indicated a requirement to use measurements for setting the dipole currents. An alternative (faster) way to generate transfer was tested. For these maps (MS+Enge FF maps) the well-known Enge functions were used for the fringe field approximation and a long multipole approximation was used for the description of transversal non-uniformities.

The MS+Enge FF maps turned out to be in fair agreement with the more accurate maps obtained via the developed approach (3D maps) for the considered dipole. However, for the dispersion element $(x|\delta)$ of the maps a significant difference of 2% was observed. The optimal multipole settings obtained using 3D maps and MS+Enge FF maps were slightly different, which though did not affect the resulting phase space distributions at the focal planes of the preseparator significantly.

Further investigations with 3D magnetostatic simulations are needed to reach an even better agreement between measured and simulated magnetic field data. Firstly, adjustment of the input virgin curve for low H values can bring a better agreement of measurements and simulations for magnets with unipolar power supplies. Secondly, the yoke could be divided into subblocks for description of their magnetization by various $B-H$ curves depending on their maximal H values. More desirable would be to have the remanence phenomenon considered in the commercial 3D FEM solvers. Other possibilities to extend the SIHM algorithm for flat volumes should be studied, in order to simplify the resulting workflow. This could be, for example, involving of dedicated least squares fitting into the integrand computations.

Considering the ion-optical simulations, further development and study of approaches like MS+Enge FF have to be carried out. A smooth piecewise polynomial approximation of the fringe field should be tested at first. Next, the applicability of the MS+Enge FF method to quadrupoles should be studied. The concept of the equivalent hard-edge length has to be applied to multipoles to obtain transfer maps dependent on the coil current. These transfer maps will provide the desired integral gradients independent on the yoke saturation. A detailed error study and optimization of the algorithm to generate 3D transfer maps could be performed in order to reduce numerical errors.

A collaboration with CERN is planned for measuring 3D magnetic field of a dipole for further tests of the SIHM method. If the method can be approved by the tests, which is mostly endangered by systematic measurements errors, it has a potential to be established within the separator community, since it provides a fast interface between the magnetic measurements and ion-optical simulations. In cooperation with the Center for Beam Theory And Dynamical Systems at Michigan State University the developed methods are going to be implemented into the official beam physics package of COSY INFINITY.

In future, the developed method is going to be applied to all of the 26 different magnet types of the Super-FRS starting from the short quadrupole for which the saturation of the yoke is maximal [7, 69]. The expected influence of the short quadrupole saturation on the beam dynamics is at least one order of magnitude larger than the impact of the NC dipole saturation. The already adapted code for the automated optimization of the Super-FRS preseparator is going to be extended to consider the entire Super-FRS.

List of Symbols

Term	Unit	Description
A	Tm	Magnetic vector potential
a	rad	Relative transversal horizontal angle ($a = p_x/p_s$)
$\vec{B}$	T	Magnetic flux density
B_0	T	Central magnetic flux density of a dipole magnet
$B\rho$	Tm	Particle magnetic rigidity
b	rad	Relative transversal vertical angle ($b = p_y/p_s$)
β	1	Velocity divided by speed of light ($\beta = v/c$)
c	m/s	Speed of light in vacuum
$\Delta_{\mathcal{M},\mathrm{tr}}$	1	Relative difference in the coordinates for tracking and transfer map evaluation
δ	1	Relative momentum deviation ($\delta = \frac{E_k - E_{k,0}}{E_{k,0}}$)
$\vec{E}$	V/m	Electric field strength
E_k	J	Kinetic energy
E_0	J	Rest energy
e	C	Charge of electron
η	1	Ratio of kinetic to rest energy ($\eta = E_k/E_0$)
$\vec{F}$	N	Force
ϕ	Tm	Magnetic scalar potential
γ	1	Relativistic factor
$\vec{H}$	A/m	Magnetic field strength
I	A	Electric current
L_{eff}	m	Effective length of ion-optical element
L_{eq}	m	Equivalent hard-edge length of ion-optical element
l	1	Relative time-of-flight deviation ($l = \frac{-(t-t_0)v_0\gamma}{(1+\gamma}$))
m	kg	mass
$\mathcal{M}$		Taylor transfer map
μ_0	Tm/A	Vacuum permeability
μ_r	1	Relative magnetic permeability
p	$kg \cdot m/s$	Particle momentum

Term	Unit	Description
q	C	Charge of particle
R	m	Radius of deflection
$\vec{r}$	m	Position vector ($\vec{r} = (X, Y, Z)$)
s	m	Independent beam physics variable (arclength)
t	s	Time
θ	°	angle of deflection
v	m/s	Particle velocity
x	m	Relative transversal horizontal coordinate
y	m	Relative transversal vertical coordinate

List of Acronyms

BINP Budker Institute of Nuclear Physics.

CERN Conseil européen pour la recherche nucléaire.

DA Differential algebra.

FAIR Facility for Antiproton and Ion Research in Europe GmbH.

FEM Finite elements method.

FWHM Full width at half maximum.

GSI GSI Helmholtzzentrum für Schwerionenforschung GmbH.

IEC Integrated excitation current.

LS Least squares.

NC Normal conducting.

NUSTAR Nuclear Structure Astrophysics and Reactions.

ODEs Ordinary differential equations.

rms Root mean square.

SIHM Surface integration Helmholtz method.

Super-FRS Superconducting Fragment Separator.

TOF Time of flight.

TPSA Truncated power series algebra.

TRAFIC Tracking particles and Fitting Coefficients.

List of Figures

List of Tables

Bibliography

[1] C. Scheidenberger, "Collaboration report NUSTAR progress in 2013," *Scientific Report 2013, GSI Helmholtzzentrum für Schwerionenforschung*, vol. 2014-1, pp. 95–97, 2014. 1

[2] G. Münzenberg and H. Geissel, "NUSTAR – presence and prospects of nuclear structure research at GSI and FAIR," *J. Phys.: Conf. Ser.*, vol. 413, p. 012006, 2013. 1

[3] GSI Helmholtzzentrum für Schwerionenforschung GmbH and Facility for Antiprotonen and Ion Research in Europe, eds., *GSI-FAIR Scientific Report 2017*. No. GSI Report 2018-1, GSI-2017-01856, Darmstadt: GSI Helmholtzzentrum für Schwerionenforschung, 2018. 1, 3

[4] Facility for Antiproton and Ion Research in Europe GmbH. Website: https://fair-center.de, accessed on 2019-01-19. 1, 3, 91

[5] D. J. Morrissey and B. M. Sherrill, *The Euroschool Lectures on Physics with Exotic Beams, Vol. I*, ch. In-Flight Separation of Projectile Fragments. 2004. 1

[6] H. Geissel *et al.*, "The Super-FRS project at GSI," *Nucl. Instrum. Methods Phys. Res. B*, vol. 204, pp. 71–85, 2003. 1

[7] H. Geissel *et al.*, *Technical Design Report on the Super-FRS*. No. GSI-2013-05264, Darmstadt: NUSTAR, 2008. 1, 44, 85

[8] M. Ferrario, M. Migliorati, and L. Palumbo, "Space Charge Effects," in *Proceedings of CAS - CERN Accelerator School: Advanced Accelerator Physics Course: Trondheim, Norway, August 18-29, 2013*, pp. 331–356, 2014. 1

[9] J. R. Rees, *Symplecticity in Beam Dynamics: An Introduction*. No. SLAC-PUB–9939, United States: SLAC. 1

[10] M. Berz, *Modern map methods in particle beam physics*. San Diego and others: Academic Press, 1999. 1, 2, 12, 13, 17, 50

[11] H. Wollnik, *Optics of Charged Particles*. San Diego and others: Academic Press, 1987. 1, 50, 51

[12] M. Berz, "Arbitrary order description of arbitrary particle optical systems," *Nucl. Instrum. Methods Phys. Res. A*, vol. 298, pp. 426–440, 1990. 2, 13, 14

[13] M. A. J. van der Stam and P. Kruit, "A general framework for numerical calculation of properties of charged-particle optical systems," *Nucl. Instrum. Methods Phys. Res. A*, vol. 427, no. 1, pp. 368 – 374, 1999. 2

[14] B. Schillinger, *Ionenoptik mit numerischer Streufeldanalyse*. PhD thesis, Technische Universität Darmstadt, Darmstadt, 1999. 2

[15] B. Hartmann, *Analytische Bestimmung von Bildfehlern im Streufeldbereich ionenoptischer Elemente*. PhD thesis, Justus-Liebig-Universität Gießen, Gießen, 1992. 2

[16] S. Manikonda, *High Order Finite Element Methods to Compute Taylor Transfer Maps*. PhD thesis, Michigan State University, 2006. 2, 16

[17] S. Manikonda and M. Berz, "Multipole expansion solution of the Laplace equation using surface data," *Nucl. Instrum. Methods Phys. Res. A*, vol. 558, pp. 175–183, 2006. 2, 16

[18] C. Muehle, D. Gurov, N. Khavin, Y. Kolokolnikov, G. Moritz, A. Utkin, P. Vobly, C. Will, and M. Winkler, "Radiation resistant prototype dipole for the first stage of super-frs," *IEEE Trans. Appl. Supercond.*, vol. 22, no. 3, p. 4003304, 2012. 2, 23

[19] "CST EM Studio." Website: https://www.cst.com/products/cstems, accessed on 2019-01-19. 3, 9

[20] K. Makino and M. Berz, "COSY INFINITY Version 9," *Nucl. Instrum. Methods Phys. Res. A*, vol. 558, pp. 346–350, 2006. 3, 11, 16

[21] J. M. Peña and T. Sauer, "On the multivariate horner scheme," *SIAM J. Numer. Anal.*, vol. 37, pp. 1186–1197, 2000. 3

[22] "GSI Helmholtzzentrum für Schwerionenforschung." Website: www.gsi.de, accessed on 2019-01-19. 3

[23] H. Geissel and others, "The GSI projectile fragment separator (FRS): a versatile magnetic system for relativistic heavy ions," *Nucl. Instrum. Methods Phys. Res. B*, vol. 70, pp. 286 – 297, 1992. 3

[24] H. Geissel and C. Scheidenberger, "Slowing down of relativistic heavy ions and new applications," *Nucl. Instrum. Methods Phys. Res. B*, vol. 136-

138, pp. 114 – 124, 1998. 4

[25] J. S. Winfield *et al.*, "A versatile high-resolution magnetic spectrometer for energy compression, reaction studies and nuclear spectroscopy," *Nucl. Instrum. Methods Phys. Res. A*, vol. 704, pp. 76 – 83, 2013. 4

[26] C. Brandau *et al.*, "Status of the energy-buncher in the low-energy branch of the Super-FRS," *Eur. Phys. J. Special Topics*, vol. 150, no. 1, pp. 225–226, 2007. 4

[27] A. W. Chao, K. H. Mess, M. Tigner, and F. Zimmermann, *Handbook of Accelerator Physics and Engineering*. WORLD SCIENTIFIC, 2013. 6

[28] H. Wiedemann, *Particle Accelerator Physics*. Springer International Publishing, 2015. 6

[29] R. M. Bozorth, *Ferromagnetism*, ch. The Magnetization Curve and the Domain Theory. Piscataway, United States: Wiley-IEEE Press, 1978. 8

[30] "Opera Simulation Software: Magnetostatic module." Website: https://operafea.com/product/solutions-modules/magnetostatics/, accessed on 2019-01-19. 9

[31] "COMSOL: AC/DC module." Website: https://www.comsol.com/acdc-module, accessed on 2019-01-19. 9

[32] "Ansys Maxwell." Website: https://www.ansys.com/de-de/products/electronics/ansys-maxwell, accessed on 2019-01-19. 9

[33] K. L. Brown, *The Ion Optical Program TRANSPORT*. No. 91, Menlo Park, United States: SLAC, 1979. 11

[34] M. Berz, H. C. Hoffmann, and H. Wollnik, "COSY 5.0 — The fifth order code for corpuscular optical systems," *Nucl. Instrum. Methods Phys. Res. A*, vol. 258, pp. 402 – 406, 1987. 11

[35] "GICOSY." Website: https://web-docs.gsi.de/~weick/gicosy/, accessed on 2019-01-19. 11

[36] "MAD: Methodic accelerator design." Website: http://mad.web.cern.ch/mad/, accessed on 2019-01-19. 11

[37] K. Hirata, "An introduction to SAD," in *Proceedings of the 2nd Advanced ICFA Beam Dynamics Workshop on Aperture-Related Limitations of the Performance and Beam Lifetime in Storage Rings: Lugano, Switzerland, April 11-16, 1988*, pp. 62–65, 1988. 11

[38] F. Méot, "The ray-tracing code Zgoubi," *Nucl. Instrum. Methods Phys. Res. A*, vol. 427, pp. 353 – 356, 1999. 11

[39] M. Berz and K. Makino, "COSY INFINITY 10.0 Programmer's Manual," 2017. 11

[40] M. Berz and K. Makino, "COSY INFINITY 10.0 Beam Physics Manual," 2017. 11, 36, 50

[41] M. Berz, K. Makino, and W. Wan, *An Introduction to Beam Physics*. Series in High Energy Physics, Cosmology and Gravitation, CRC Press, Taylor & Francis Group, 2014. 12

[42] K. Makino, *Rigorous analysis of nonlinear motion in particle accelerators*. PhD thesis, Michigan State University, Michigan, 1998. 12

[43] A. Chao, *Lecture notes on topics in accelerator physics*. No. SLAC-PUB-9574, Stanford, United States: SLAC, 2002. 16

[44] R. Plonsey and R. E. Collin, *Principles and applications of electromagnetic fields*. McGraw-Hill series in electrical engineering: Electromagnetics, United states: McGraw-Hill, 1961. 16

[45] J. Aldrich, "Doing Least Squares: Perspectives from Gauss and Yule," *Int. Stat. Rev.*, vol. 66, pp. 61–81. 17

[46] C. Runge, "Über empirische Funktionen und die Interpolation zwischen äquidistanten Ordinaten," *Z. Math. Phys.*, vol. 46, p. 224–243, 1901. 19

[47] W. Gander, M. J. Gander, and F. Kwok, *Scientific Computing - An Introduction using Maple and MATLAB*, ch. Least Squares Problems, pp. 261–385. Springer International Publishing, 2014. 19

[48] J. Stoer, "On the numerical solution of constrained least-squares problems," *SIAM J. Numer. Anal.*, vol. 8, pp. 382–411, 1971. 19

[49] E. M. S. Springer Verlag GmbH, "Lagrange multipliers. encyclopedia of mathematics." Website: http://www.encyclopediaofmath.org/index.php?title=Lagrange_multipliers&oldid=32304, accessed on 2019-01-19. 19

[50] The Budker Institute of Nuclear Physics SB RAS, *Magnet measurement report GSI dipole magnet*. No. DI-008-001-10-BU, Novosibirsk, Russia: BINP, 2010. 23, 25

[51] E. Kazantseva, O. Boine-Frankenheim, H. Weick, M. Berz, and K. Makino, "Accurate taylor transfer maps for large aperture iron dominated magnets used in charged particle separators and spectrometers," *Submitted to Nucl. Instrum. Methods Phys. Res. A*. 23, 49, 65

[52] E. Kazantseva and Boine-Frankenheim, O and Weick, H and S. Winfield, J and Berz, M and Jagasia, R and Makino, K, "BRho-Dependent Taylor Transfer Maps for Super-FRS Dipole Magnets," in *Proceedings of the 8th International Particle Accelerator Conference (IPAC'17), Copenhagen, Denmark, 14-19 May, 2017*, pp. 2631–2634. 23, 52

[53] GSI Helmholtzzentrum für Schwerionenforschung GmbH, "Parameter List of Super-FRS V3.0," 2013. 23, 24, 42, 64, 97

[54] K. N. Henrichsen, "Permeameter," in *Proceedings of the 2nd International Conference On Magnet Technology (MT'67), Abingdon, United Kingdom, 11-13 November, 1967*, pp. 735–739. 23

[55] Autodesk Inventor. Website: https://www.autodesk.com/products/inventor/overview, accessed on 2019-01-19. 25

[56] B. Erdélyi, M. Berz, and M. Lindemann, "Differential Algebra Based Magnetic Field Computations and Accurate Fringe Field Maps," *Vestnik St. Petersburg University, Mathematics*, vol. 10, pp. 36–55, 2015. 34

[57] E. Hille, *Analytic function theory, Vol. I*. New York, United States: Chelsea Publishing Company, 1959. 38

[58] K. Makino, M. Berz, and C. Johnstone, "High-Order Out-of-Plane Expansion for 3D Fields," *Int. J. Mod. Phys.*, vol. A26, pp. 1807–1821, 2011. 43, 47

[59] K. Makino, "The COSY 8th order Runge-Kutta integrator." 49

[60] M. Berz, B. Erdélyi, W. Wan, and K.-Y. Ng, "Differential algebraic determination of high-order off-energy closed orbits, chromaticities, and momentum compactions," *Nucl. Instrum. Methods Phys. Res. A*, vol. 427, pp. 310–314, 1999. 49

[61] P. Prince and J. Dormand, "High order embedded Runge-Kutta formulae," *J. Comput. Appl. Math.*, vol. 7, pp. 67 – 75, 1981. 57

[62] H. Geissel, H. Weick, M. Winkler, G. Münzenberg, and M. Yavor, "Ion-optical layout of a powerful next-generation pre-separator for in-flight separation of relativistic rare isotopes," *Nucl. Instrum. Methods Phys. Res.*

B, vol. 247, pp. 368 – 376, 2006. 65, 68

[63] J. J. Moré, "The Levenberg-Marquardt algorithm: Implementation and theory," in *Proceedings of the 7th Conference on numerical analysis, Dundee, UK, 28 Jun 1977* (G. A. Watson, ed.), pp. 105–116, Springer Berlin Heidelberg, 1978. 68

[64] J. Lindhard and A. H. Sorensen, "Relativistic theory of stopping for heavy ions," *Phys. Rev. A*, vol. 53, pp. 2443–2456, 1996. 73

[65] R. P. Brent, *Algorithms for Minimization Without Derivatives (Dover Books on Mathematics)*. Mineola, United States: Dover Publications, 2013. 76

[66] E. Jones, T. Oliphant, P. Peterson, *et al.*, "SciPy: Open source scientific tools for Python." Website: http://www.scipy.org/, accessed on 19.01.2019. 76

[67] D. Zangrando and R. P. Walker, "A stretched wire system for accurate integrated magnetic field measurements in insertion devices," *Nucl. Instrum. Methods Phys. Res. A*, vol. 376, pp. 275 – 282, 1996. 76

[68] S. H. Kim, C. Doose, R. Hogrefe, K. Kim, and R. Merl, "The Magnet measurement facility for the Advanced Photon Source," *IEEE Trans. Magn.*, vol. 30, pp. 2616–2619, 1994. 76

[69] E. J. Cho and others, "Magnetic Design for the Superferric Multipole Magnets of the Super-FRS," *IEEE Trans. Appl. Supercond.*, vol. 28, pp. 1–5, 2018. 85

Acknowledgement

First of all I would like to express my gratitude to Prof. Dr. Oliver Boine-Frankenheim for accepting me as a PhD student and for guiding and encouraging me through the years of my work. Secondly, I want to thank Prof. Dr. Christoph Scheidenberger for agreeing to be my second referent and for the fruitful discussions during our HGS-HIRe meetings.

Next, I would like to express my deep appreciation to Dr. Helmut Weick for supervising me. This work would be inconceivable without his irreplaceable help and constructive feedback.

I thank Prof. Dr. Martin Berz and Prof. Dr. Kyoko Makino as well as their PhD student Ravi Jagasia from Michigan State University for their priceless help on understanding differential algebra and COSY as well as for the subsequent collaboration. The three weeks that I spent at MSU as a guest student were enriched with a lot of fruitful discussions, which brought me a solid basis for the success in the future research.

I am grateful to Dr. John Winfield for his help with the Super-FRS ion-optical codes as well as for supporting me with all the data that I needed for my work.

A special “thank you” I want to say to the members of the GSI NC magnetic group. I thank Dr. Hanno Leibrock and Dr. Carsten Mühle for their friendliness and help with the model of the NC magnet. Also I want to thank Dr. Peter Rottländer for his support regarding the Opera Vector Field software. I am very grateful to Dr. Franz Klos for the measurements of the magnetic permeability and for the discussions during the automated measurement processes.

I am thankful to my internal and external TEMF colleges and ex-colleges for a nice working atmosphere. I want to thank Wolfgang

Ackermann for his support regarding the CST EMS code, Wolfgang Müller and Dragos Munteanu for their help with technical and organizational questions. I am thankful to Prof. Dr. Herbert De Gersem as well as Thilo Egenolf for their valuable comments on this manuscript. My special gratitude goes to Heike Koch for making me a nice company during the back training and to Achim Wagner for taking care of the coffee-machine and travel reimbursement. I want to thank TEMF and GSI for financing my conferences and workshops, which gave me a possibility for useful scientific exchange and collaboration.

I am thankful to my friends and my family for their mental support and understanding. I owe my gratitude to my boyfriend Stephan for his endless patience, care and support during this tough period of my life.